nature methods

Article

https://doi.org/10.1038/s41592-025-02867-0

Scalable spatial single-cell transcriptomics and translatomics in 3D thick tissue blocks

Received: 29 July 2024

Accepted: 15 September 2025

Published online: 24 November 2025

Check for updates

Xin Sui[1,2,6], Jennifer A. Lo[2,3,6], Shuchen Luo[1,2], Yichun He[2,4,5], Zefang Tang[1,2], Zuwan Lin[2,4], Dániel L. Barabási[2,5], Yiming Zhou[1,2], Wendy Xueyi Wang[1,2,4], Jia Liu[4] & Xiao Wang[1,2]

Characterizing the transcriptional and translational gene expression patterns at the single-cell level within their three-dimensional (3D) tissue context is essential for revealing how genes shape tissue structure and function in health and disease. However, most existing spatial profiling techniques are limited to 5–20 µm thin tissue sections. Here, we developed Deep-STARmap and Deep-RIBOmap, which enable 3D in situ quantification of thousands of gene transcripts and their corresponding translation activities, respectively, within 60–200-µm thick tissue blocks. This is achieved through scalable probe synthesis, hydrogel embedding with efficient probe anchoring and robust cDNA crosslinking. We first utilized Deep-STARmap in combination with multicolor fluorescent protein imaging for simultaneous molecular cell typing and 3D neuron morphology tracing in the mouse brain. We also demonstrate that 3D spatial profiling facilitates comprehensive and quantitative analysis of tumor–immune interactions in human skin cancer.

The spatial regulation of gene expression and translation is critical for tissue function[1–6]. In situ profiling technologies enable the study of both the transcriptome and translatome within their original spatial contexts[7–10]; however, most spatial omics techniques are confined to analyzing thin tissue sections (5–20 µm)[11]. Many functional and anatomical studies in tissue biology require 3D profiling in tissue blocks across multiple cellular layers[12,13]. For instance, in neuroscience, 3D morphological profiling and long-range projection mapping[14–17], in situ electrophysiology[18–23] and in vivo neural activity imaging[24–26] in the brain require direct measurements in 3D brain volumes (100–300 µm) where thin tissue sections are inadequate. In cancer pathology, 3D samples offer a more accurate representation of tumor architecture, microenvironment and cell–cell interactions in patient samples[27].

Although reconstructing 3D volumes using serial thin sections is feasible, this method faces three important challenges. First, tissue sectioning often fragments cells, resulting in partial RNA readouts, complicating the accurate analysis of the transcriptome. Second, tissue deformation during sectioning presents a persistent challenge for computational reconstruction methods. Third, this approach requires substantial manual labor. Therefore, developing effective spatial omics methods for 3D profiling from thick tissue blocks is imperative.

Current thick-tissue spatial profiling approaches achieve quantitative in situ measurements of transcriptome in thick samples using single or multi-round fluorescence in situ hybridization (FISH)[28–41], but are limited in several aspects. The number of genes they can analyze is typically fewer than 300, and the size of the imaging areas is often restricted to a single brain region. These limitations arise primarily because these methods often employ linear coding instead of exponential coding, and rely on RNA integrity to preserve the imaging signal, substantially reducing their efficiency of RNA detection, scalability of gene numbers and tissue volume, and flexibility of sample handling and imaging time[29–41]. Additionally, the displacement of RNA molecules between imaging rounds further restricts the number of imaging cycles that can be performed[28]. Moreover, current thick-tissue spatial

[1]Department of Chemistry, Massachusetts Institute of Technology, Cambridge, MA, USA. [2]Broad Institute of MIT and Harvard, Cambridge, MA, USA. [3]Department of Dermatology, Beth Israel Deaconess Medical Center and Harvard Medical School, Boston, MA, USA. [4]John A. Paulson School of Engineering and Applied Sciences, Harvard University, Cambridge, MA, USA. [5]Eric and Wendy Schmidt Center, Broad Institute of MIT and Harvard, Cambridge, MA, USA. [6]These authors contributed equally: Xin Sui, Jennifer A. Lo. e-mail: xwangx@mit.edu

profiling methods are limited to mapping spatial transcriptomics and lack the capability to map the translatome, thus hindering multiplexed characterization of gene translation at single-cell resolution.

Here, we have developed Deep-STARmap and Deep-RIBOmap to address the aforementioned limitations by introducing a new and scalable strategy for probe synthesis and embedding as well as robust complementary DNA amplicons crosslinking, enabling scalable in situ quantification of thousands of RNA transcripts and their respective translational activities within large, intact thick tissue samples. Utilizing Deep-STARmap and Deep-RIBOmap, we profiled the transcription and translation of 1,017 genes in intact mouse brain tissue at 320 × 320 × 700 nm^3 voxel size within a thick hydrogel–tissue scaffold, revealing heterogeneity in protein translation across cell types. Additionally, by combining our method with multicolor fluorescence labeling (Tetbow)[15], we simultaneously profiled neuronal morphology and molecular signatures in single cells, achieving multimodal mapping of the adult mouse brain in a scalable manner. Last, we demonstrated the applicability of our method on human cutaneous squamous cell carcinoma (cSCC) samples, uncovering tumor–immune interactions with more accurate and quantitative spatial distributions compared to thin tissue analyses. We anticipate that Deep-STARmap and Deep-RIBOmap will yield noteworthy biological insights into the pathophysiology of cancers and other diseases.

Results

Deep-STARmap and Deep-RIBOmap workflow

We designed the workflow of Deep-STARmap and Deep-RIBOmap (Fig. 1a) as follows. It begins with the hybridization of predesigned oligonucleotide probe sets to target either all RNA molecules of a gene or ribosome-bound RNAs, respectively, in PFA-fixed tissues followed by hydrogel matrix embedding. The samples are then subjected to protein digestion and lipid removal to enhance enzyme penetration, ensuring sufficient depth coverage in thick tissue samples. Subsequently, in situ cDNA amplicons are synthesized through enzymatic ligation and rolling-circle amplification (RCA). Each cDNA amplicon contains a predesigned gene-specific identifier, which is finally decoded through cyclic sequencing, imaging and stripping steps (sequencing with error reduction by dynamic annealing and ligation (SEDAL) sequencing[31]). In comparison with a previously published thick-tissue STARmap protocol (linear encoding, 28 genes), the new developments of Deep-STARmap and Deep-RIBOmap solved the issues of scalable probe preparation, cDNA amplicon anchoring, signal decay and translation mapping capability as detailed below.

STARmap employs a padlock probe, designed to target specific messenger RNA species of interest, along with a primer that binds to the same mRNA transcript adjacent to the padlock probe binding site. In the previous publication of the STARmap protocol adapted for thick tissue[31], each primer contains a 5′ Acrydite modification to anchor the probe into the hydrogel; however, this modification is expensive to synthesize and not scalable for large gene numbers. In this report, Deep-STARmap incorporates a common 'flanking linker sequence' at the 5′ end of all primers. This addition enables an Acrydite-modified adaptor to hybridize and covalently crosslink with the flanking linker, allowing the whole probe set of primers to be conjugated to polyacrylamide hydrogels during polymerization (Fig. 1b). Covalent crosslinking is achieved with a nucleoside analog, 3-cyanovinylcarbazole nucleoside (^{CNV}K)[42], incorporated into the adaptor. Upon 366 nm UV-A irradiation, the ^{CNV}K-containing adaptor undergoes rapid photocrosslinking to the complementary strand via [2 + 2] cycloaddition with an adjacent pyrimidine base, a process shown to be nondamaging to DNA[43,44]. Experimental optimization revealed that an adaptor-to-primer ratio of 5:1 is sufficient for complete conversion of primer, and higher ratios do not increase the number of amplicons in mouse brain samples (Extended Data Fig. 1a–c). Notably, probes with a photocrosslinked 5′ Acrydite adaptor performed equivalently to those with 5′ Acrydite modifications incorporated during solid phase synthesis (Fig. 1c). It is worth noting that the photocrosslinked adaptor approach is markedly more efficient and scalable, as it employs a universal flanking linker sequence and corresponding adaptor for all primers to allow pooled synthesis. In contrast, attachment of 5′ Acrydite for each individual probe during solid phase synthesis is extremely costly, especially in the setting of >4,000 probes with up to 70 bases in length (>US$400,000; in contrast, adaptors only cost <US$200). Due to its high multiplexing capability, our method enables the embedding of a large number of probe sets into the hydrogel, expanding the number of targetable RNA species from dozens to thousands. Our findings demonstrate that UV crosslinking significantly enhances probe incorporation efficiency, resulting in a higher detection yield of cDNA amplicons compared to mere adaptor–primer hybridization. This method substantially outperforms the approach of relying solely on hydrogel physical retention (Fig. 1c). We also demonstrated that anchoring probe sets into the hydrogel is more efficient than the previously reported strategies[41,45,46] of anchoring RNA molecules into the hydrogel in our experimental setting (Extended Data Fig. 1d–g).

After hydrogel polymerization using a mixture of redox initiator and thermal initiator to embed the tissue and polymerizable primers (Extended Data Fig. 1h, i), we performed protein digestion, enzymatic ligation and RCA to construct in situ cDNA amplicons. We observed that primer polymerization alone could not efficiently retain cDNA amplicons as puncta for more than four imaging cycles, potentially because they are prone to displacement, disassembly and even fragmentation caused by buffer-dependent hydrogel expansion and contraction

Fig. 1 | Deep-STARmap and Deep-RIBOmap enable spatiotemporally resolved transcriptomics and translatomics in 200-µm-thick tissue blocks. a, Schematic summary of Deep-STARmap and Deep-RIBOmap workflow. **b**, In situ sequencing of transcriptional states in thick tissue blocks. The primer, featuring a flanking linker sequence at its 5′ end, is covalently photocrosslinked (pink rhombus) to an Acrydite-modified oligonucleotide adaptor (pink). Following the preparation of thick tissue slices (Methods), the adaptor (pink)-primer (black) complex and padlock (black) probes with unique gene identifiers (red) hybridize to intracellular mRNAs (gray dashed line) within the intact tissue. The probe set is copolymerized with acrylamide, forming a DNA–gel hybrid (blue wavy lines) through the adaptor's functionalized acrylic group, followed by the removal of unbound lipids and proteins. Subsequently, in situ cDNA amplicons are constructed by enzymatic ligation and RCA and further anchored into the hydrogel network via hydrogel re-embedding. Gene barcodes are read out via cyclic in situ SEDAL sequencing. **c**, Schematics and representative fluorescent images of negative and positive control experiments in 100-µm tissue sections of the mouse cerebral cortex (left). Quantification of cell images showing the average amplicon reads per cell ($n = 4$ images from four samples per condition) (right). Red indicates DNA amplicons from four cell type markers (Supplementary Table 1). Blue indicates 4,6-diamidino-2-phenylindole (DAPI). Scale bar, 20 µm. Two-sided independent t-test, $^{***}P < 0.001$. Data are shown as mean ± s.d. **d**, Schematics and representative fluorescent tissue images of six rounds of sequencing with and without cDNA re-embedding (left). Fluorescent images show Ch1 to Ch4 (color-coded channels for barcode decoding) and cell nuclei (blue) in mouse brain slices. All images are scaled to an eight-bit intensity range from 0 to 255 to maintain consistency across conditions. Quantification of cell images showing the average amplicon retention rate after six rounds of sequencing ($n = 4$ biological replicates, two mouse brain slices and two human skin slices) (right). Two-sided independent t-test, $^{****}P < 0.0001$. Data are shown as mean ± s.d. **e**, Representative raw fluorescent tissue images across 200 µm and quantification of DNA amplicon signal intensity at different tissue depths. $n = 4$ technical replicates, each derived from independent cortical regions across four different brain slices. **f**, Deep-RIBOmap probe design; primer (black) and padlock (black) probes with unique gene identifiers (red) hybridize to intracellular mRNAs (gray dashed line), while splint probes (green) bind to the 18S rRNA of ribosomes. Both the primer and splint probe feature a flanking linker sequence at their 5′ ends and are covalently crosslinked (pink rhombus) to an Acrydite-modified oligonucleotide adaptor (pink).

https://doi.org/10.1038/s41592-025-02867-0

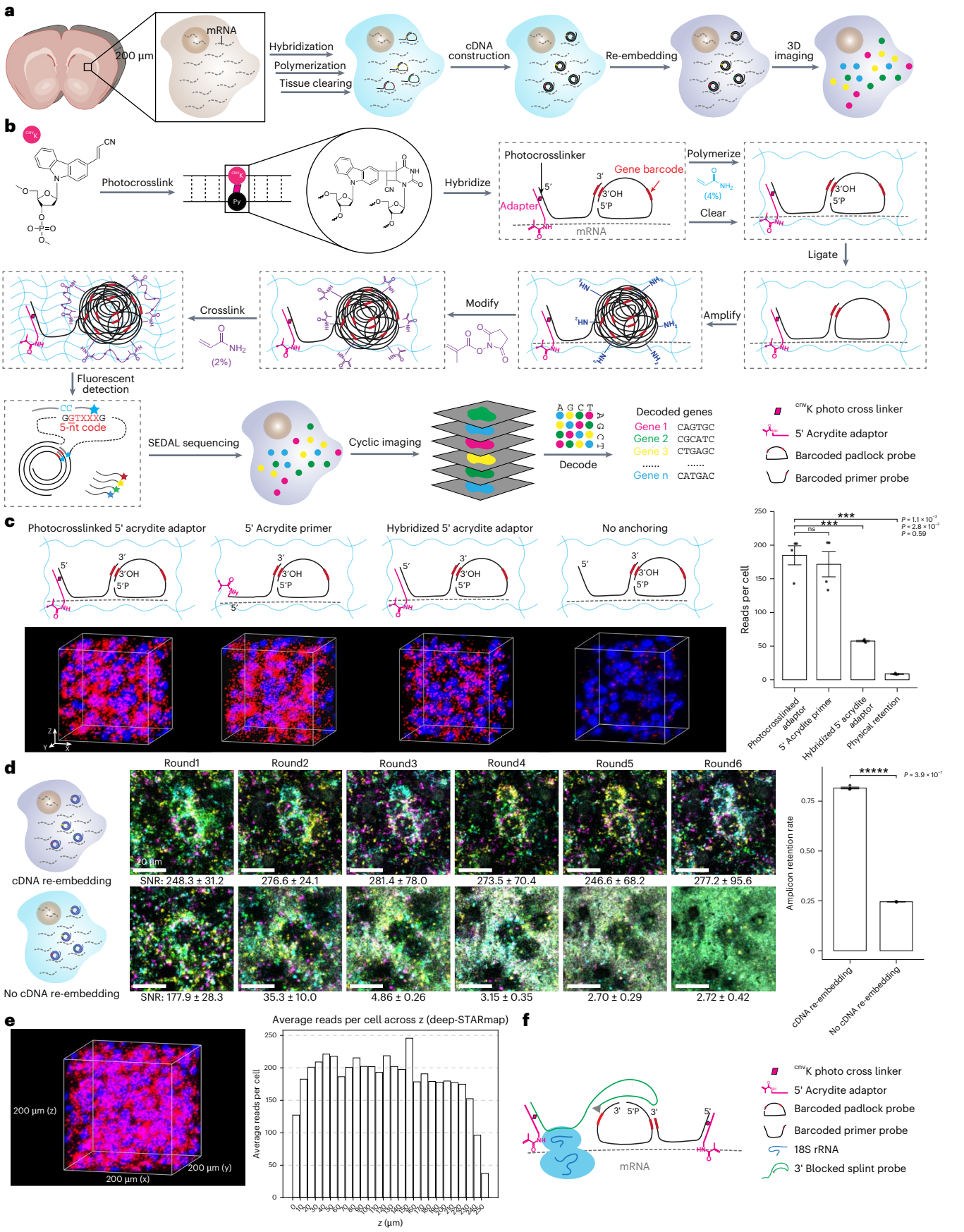

between imaging cycles, resulting in progressively lower signal-to-noise ratio (Fig. 1d). To maintain the position and integrity of the amplicons through multiple detection cycles, a second round of hydrogel embedding was introduced following RCA, which outperformed several alternative re-embedding strategies (Extended Data Fig. 2a–d). Compared to cDNA crosslinking by PEGylated bis(sulfosuccinimidyl)suberate (BSPEG), hydrogel re-embedding reduced background accumulation and improved cDNA detection efficiency. Collectively, the implementation of these strategies devised specifically for Deep-STARmap substantially enhances its robustness and scalability, enabling consistent spatial transcriptomics readouts across 200-µm-thick sections of the mouse brain (Fig. 1e and Extended Data Fig. 3a,b).

Next, we leveraged the insights gained from developing Deep-STARmap to establish Deep-RIBOmap for investigating spatial translatomics in thick tissue samples. RIBOmap utilizes a tri-probe design strategy to selectively detect and amplify ribosome-bound mRNAs: in addition to the padlock and primer, an additional splint DNA probe hybridizes to ribosomal RNAs (rRNAs)[47] and serves as splints for proximity ligation and circularization of padlock probes. Building upon this design, Deep-RIBOmap incorporates a 'flanking linker sequence' at the 5′ end of both the primer and the splint DNA probe (Fig. 1f). An Acrydite-modified adaptor covalently crosslinks to these flanking linkers, enabling the integration of the entire tri-probe set into polyacrylamide hydrogels during polymerization. Furthermore, we demonstrate spatial translatome readouts across 200-µm-thick tissue sections and show that the padlock, primer and splint probes are all crucial for signal amplification (Extended Data Fig. 3c–f). Using the same workflow as Deep-STARmap, Deep-RIBOmap achieves spatial translatomic profiling in thick tissue blocks.

Deep-STARmap and Deep-RIBOmap in mouse brain with 1,017 genes

To evaluate the scalability of Deep-STARmap and Deep-RIBOmap for high-throughput, 3D intact-tissue transcriptomic and translatomic sequencing, we applied these techniques to thick mouse brain sections (Methods), targeting a curated list of 1,017 genes (Supplementary Table 2). This gene list was compiled from reported cell-type marker genes in adult mouse central nervous system single-cell RNA sequencing (scRNA-seq) datasets and spatial transcriptomic mouse brain atlases[48–51].

We performed pairwise Deep-STARmap and Deep-RIBOmap mapping on adjacent 150-µm-thick coronal sections of the mouse hemisphere, encompassing multiple brain regions (198,675 cells for Deep-STARmap and 164,029 cells for Deep-RIBOmap). Gene identities encoded by five-nucleotide sequences on the padlock probes were read out through six rounds of sequencing by ligation with error rejection (SEDAL). Notably, the error rejection rate remained consistent across the *z*-axis (Extended Data Fig. 3g–i). To annotate cell types and align them with established nomenclature, we integrated our Deep-STARmap and Deep-RIBOmap with a published spatial brain atlas with curated cell typing annotations, using two different approaches independently. In the first approach, we used FuseMap[52], a recently developed integration method that transfers cell type annotations leveraging both spatial and cellular information (Fig. 2a). We also benchmarked the results using a second approach, where an established method, Harmony[53], is used solely relying on single-cell gene expression information (Fig. 2b). Both methods were applied independently to the same datasets and yielded consistent results: the confusion matrix of major cell type assignments showed that FuseMap's cell types were highly concordant (82.4% matched labels) with those identified by the traditional single-cell sequencing integration method (Fig. 2c and Supplementary Table 3). As FuseMap integrates multiple large-scale spatial transcriptomic datasets and cell-type annotations of the mouse brain[52] and has demonstrated higher accuracy in sublevel transferred annotations, we proceeded with FuseMap for downstream analyses.

Specifically, FuseMap integration, followed by nearest-neighbor label transfer of main-level annotations, identified 19 main cell types, including nine neuronal, five glial, one immune and four vascular cell clusters, all of which exhibited canonical marker genes and expected spatial distributions (Extended Data Fig. 4a,b). Further transfer of sublevel annotations within each main cluster resulted in 137 subclusters (Fig. 2d and Extended Data Fig. 5a)[51,54] (https://mouse.brain-map.org/). Our spatial transcription and translation patterns of canonical cell-type marker genes and neurotransmitter genes aligned consistently with previously published spatial transcriptomic and translatomic sequencing results. Based on these cell typing results, we generated spatial cell maps of the imaged hemibrain region. Our analysis revealed a high degree of concordance between Deep-STARmap and Deep-RIBOmap in terms of gene expression profiles, cell-type composition and spatial organization. The observed patterns were consistent with scRNA-seq datasets and spatial transcriptomic measurements from thin tissue sections, further validating the robustness and accuracy of our approach (Extended Data Fig. 5b,c and Extended Data Fig. 6a). We also performed a second biological replicate for Deep-STARmap and Deep-RIBOmap mapping, as well as Tetbow fluorescent protein imaging. Independent analysis shows consistent gene expression, spatial distribution and cell typing results (Extended Data Fig. 7a,b).

By exploiting the single-cell and spatial resolution of paired Deep-STARmap and Deep-RIBOmap datasets, we probed the heterogeneity in translational regulation across various cell types and brain regions. To investigate translationally regulated genes across different cell types, we first performed gene clustering using Deep-STARmap and Deep-RIBOmap profiles, identifying 18 gene modules (Extended Data Fig. 7c and Supplementary Table 4) with distinct functions and expression patterns (Extended Data Fig. 7d). Previous research has shown that non-neuronal cells, particularly oligodendrocytes, exhibit marked translational regulation[47]. We analyzed a gene module comprising 74 genes predominantly expressed across the oligodendrocyte lineage, from oligodendrocyte progenitor cells (OPCs) to mature subtypes (OLG1 and OLG2). Our findings recapitulate previous observations[47], demonstrating that genes with higher translation efficiency in mature oligodendrocytes are associated with myelination (Extended Data Fig. 7e).

Beyond our extensive transcriptome analysis of the brain, we focused on investigating translational control at the subcellular level. Translation localized to the soma and processes in brain tissue plays a pivotal role in the organization and plasticity of neuronal and glial networks in response to physiological stimuli during neurodevelopment and memory formation (Extended Data Fig. 8a). To dissect this localized translation, we categorized Deep-RIBOmap reads in 3D thick tissue blocks into somata-localized reads (within the cell body, identified using Watershed 3D[55]) and processes-localized reads (the rest of the reads). We then identified the top 10% of genes with the highest and lowest processes-to-somata ratios, designating them as enriched in processes and somata, respectively (Extended Data Fig. 8b–d and Supplementary Table 5). Gene Ontology (GO) analysis indicated that genes enriched in processes are involved in the cell projection, cell junction and cell–cell signaling, while those enriched in somata are associated with the extracellular matrix and various receptors (Extended Data Fig. 8c).

Given the ability of Deep-STARmap and Deep-RIBOmap to measure multiple layers of cells, we next tested whether our methods could resolve volumetric patterns of cell organization in 3D. We performed a detailed analysis of the nearest-neighbor distances among various interneuron subtypes. Previous studies have demonstrated that interneurons of identical subtypes frequently form juxtaposed pairs in the mouse visual cortex. Our result substantiates these findings, indicating that an inhibitory neuron is predominantly adjacent to another of the same subtype (Lamp5, Vip, Sst or Pvalb) rather than other inhibitory subtypes (Extended Data Fig. 8e,f and Supplementary Table 6), a pattern more accurately captured in 3D than in two dimensions (2D) (Extended Data Fig. 8f,g). This close spatial proximity may be related

https://doi.org/10.1038/s41592-025-02867-0

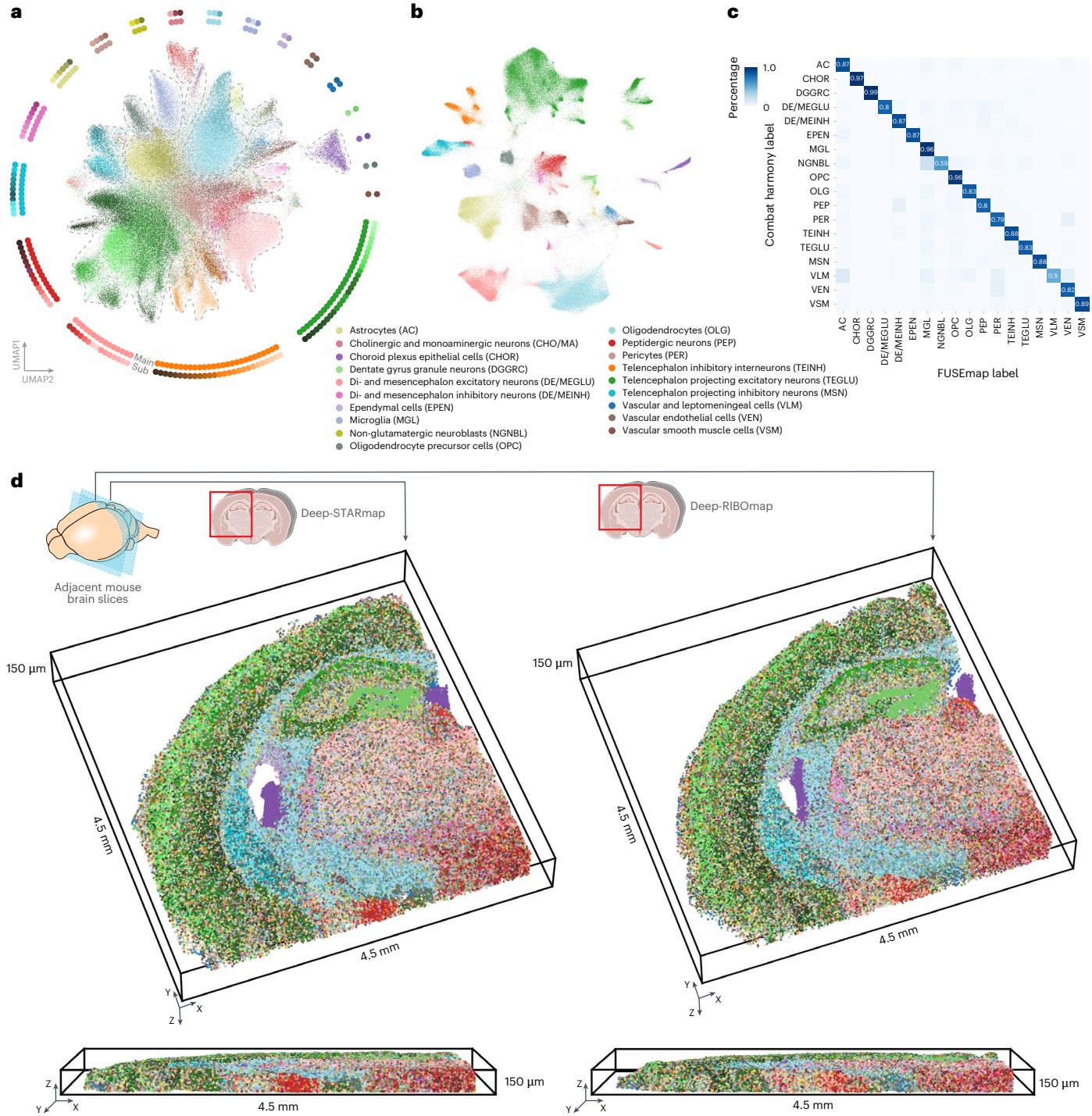

Fig. 2 | Spatial single-cell transcriptomic and translatomic profiling of 1,017 genes in thick mouse brain slices. a,**b**, UMAP plot visualizations of transcriptional and translational profiles of 362,704 cells collected from mouse coronal hemibrains using FuseMap (**a**) and integration using Harmony (**b**). Surrounding diagrams display 137 subclusters derived from 19 main clusters. **c**, Confusion matrix of cell type labels obtained from FuseMap and Harmony integration, visualizing cell types with more than 100 cells in the sample. **d**, 3D molecular cell-type maps derived from Deep-STARmap (left) and Deep-RIBOmap (right) across adjacent 150-µm-thick sections from the mouse hemisphere. Each dot represents one cell, colored by its subcluster identity, using the same color code as in **a**.

to the formation of gap junctions, which are crucial for synchronized firing patterns and may enhance visual responses in the cortex[56–58].

Single-cell morphology analysis of molecular cell types with Tetbow

Understanding brain function necessitates a detailed mapping of its neuroanatomy. Electron microscopy (EM) remains the gold standard for neuroanatomical studies, offering nanometer-scale resolution[59,60]. However, EM reconstructions are largely incompatible with molecular cell typing, resulting in a trade-off between spatial resolution and molecular information. Additionally, the current analytical throughput of EM is inadequate for studying the long-range spatial organization of mouse and mammalian neurons. The integration of stochastic multicolor labeling techniques[14,15,61] with spatial

https://doi.org/10.1038/s41592-025-02867-0

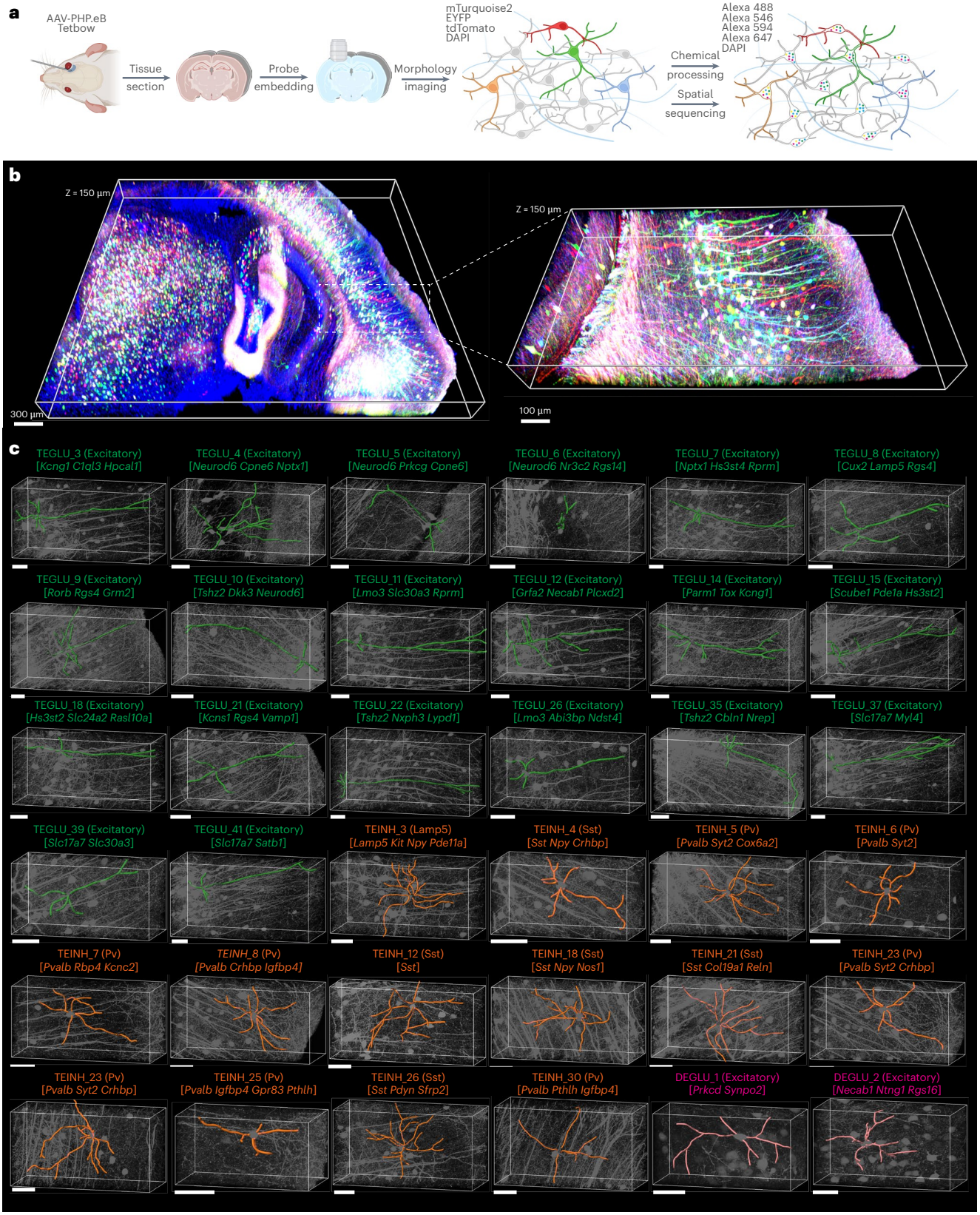

Fig. 3 | Characterizing the morphological features of transcriptomic types. a, DeepSTARmap combined with Tetbow enables simultaneous profiling of gene expression and neuron morphologies. **b**, Volume rendering of neurons in the hippocampus and thalamus labeled with Tetbow (left). Neurons exhibit unique colors generated by the stochastic and combinatorial expression of three fluorescent proteins (tdTomato, EYFP and mTurquoise2), enabling the high-resolution identification and differentiation of individual neurons. Zoom-in view of volume rendering of mouse cortical pyramidal neurons labeled with Tetbow (right). **c**, Representative individual morphological reconstructions of different transcriptome-defined subtypes of excitatory and inhibitory neurons. Scale bar, 50 μm.

transcriptomic mapping offers a promising solution. This combined approach enables the generation of comprehensive co-profiling of the transcriptome and morphology of individual neurons within densely labeled neural circuits.

To simultaneously interrogate transcriptomic readouts and morphology within single cells by exploiting the unique advantages of thick tissue mapping, we integrated the stochastic multicolor genetic labeling tool, Tetbow[15], into our workflow (Fig. 3a). Tetbow enables bright and high-resolution mapping of intermingled neurons in situ by tagging individual neurons with stochastic combinations of three cytoplasmically localized fluorescent proteins. It has also been demonstrated that systemically delivered adeno-associated viruses (AAVs) allow a more uniform distribution of labeled cells and color diversity[62]. Thus, we utilized the AAV-PHP.eB[62] variant to coadminister three separate vectors encoding three fluorescent proteins, along with a tetracycline-off transactivator (tTA) expression vector to activate combinatorial fluorescent protein expression across the entire brain (Fig. 3b and Extended Data Fig. 9a).

Following tissue sectioning and probe-hydrogel embedding, we performed imaging for the three Tetbow fluorescent proteins (FPs) along with 4,6-diamidino-2-phenylindole (DAPI) and observed bright, high-quality labeling of diverse neuronal cell types across all regions of the brain (Fig. 3a). Following morphology imaging, we digested the FPs from the sample using tissue clearing to enable subsequent transcriptome profiling of 1,017 genes. cDNA amplicons were constructed and sequenced as previously described. We additionally used DAPI as a fiducial marker for image registration between the two imaging modalities to correspond each FP-labeled neuron to its molecular subtype identity resolved by Deep-STARmap (Extended Data Fig. 9b,c and Supplementary Table 7).

To visualize the morphological diversity of labeled neurons, we implemented a semi-automated morphological reconstruction pipeline in Bitplane Imaris. As proof of concept, we reconstructed the dendritic arbors of 50 principal cells and interneurons across the imaged volumes, together spanning 37 molecular subtypes pooled from two biological replicates with different viral titers (Fig. 3c). We focused our study on the dendritic arbor to maximize the accuracy of our traces, as it has been demonstrated that fine axonal morphologies cannot be consistently and faithfully recapitulated without a membrane-localized marker[61]. In agreement with previous studies characterizing neuronal morphology[63,64], we resolved the characteristic dendritic trees of principal pyramidal neurons across different brain regions. Using Deep-STARmap, we identified distinct morphologies in molecularly defined neuronal subtypes, including CA1 hippocampal (TEGLU_3,7,8,9,10,11,12,14,15,18,21,22,26,35,37,39,41) and layer V neocortical pyramidal neurons (TEGLU_4,5,6). As expected, the apical dendrites of these neurons extended toward the stratum lacunosum-moleculare in CA1 and toward the cortical surface in layer V, both forming distinct tree-like structures. Similarly, despite their lower abundance, we resolved diverse dendritic morphologies of cortical GABAergic inhibitory interneurons, which exhibited a wide range of dendritic morphologies. This approach allowed us to examine further the morphological diversity of several major subclasses of GABAergic neurons[65], classified by their transcriptomic profiles, within the mouse cerebral cortex. To assess the robustness of these qualitative observations, we trained a classifier using ~70% of reconstructed neurons and tested it on the remaining 30%. The classifier accurately distinguished major neuronal classes, including excitatory pyramidal neurons, Sst interneurons and Pv interneurons based on dendritic features, confirming that transcriptome-defined subtypes correspond distinct dendritic architectures (Extended Data Fig. 9d). Thus, by integrating high-throughput spatial sequencing with neuronal morphology profiling, Deep-STARmap establishes a scalable framework for systematically investigating neuronal diversity in intact circuits.

Deep-STARmap in human cutaneous squamous cell carcinoma

Deep-STARmap's potential extends beyond neuroscience. One particularly promising application lies in the field of oncology, where a comprehensive understanding of the spatial organization of tumors, their microenvironments and immune interactions is crucial. Skin cancers account for ~90% of all human malignancies. The second-most prevalent skin cancer is cutaneous squamous cell carcinoma (cSCC), which arises from keratinocytes (the major cell type of the epidermis). Over 1 million new cSCC cases are diagnosed annually in the United States[66], with an estimated 3.7% of cSCCs leading to metastatic disease and 1.5% of cases resulting in death from disease[66]. The leading risk factor for cSCC is chronic ultraviolet radiation (UVR) exposure, which has mutagenic effects on the skin. UVR-induced somatic mutations translate to a large burden of tumor neoantigens that are thought to be responsible for the high immunogenicity of cSCCs[67]. Of note, immunosuppressed patients are at a 65–100 fold higher risk of developing cSCC and are more likely to be diagnosed with multiple and metastatic cSCCs due to a failure of cancer immunosurveillance[68,69]. Immunotherapies such as immune checkpoint inhibitors have shown promise in the treatment of advanced cSCC[70]; however, many patients fail to respond and the biomarkers, precise cell subpopulations and mechanisms underlying response versus resistance are not well understood. There is great interest in assessing the spatial organization and signaling between tumor, immune and stromal cells in the native tumor microenvironment. Previous spatial studies of cSCC have been limited to thin tissue samples that do not capture the full complexity of tumor architecture, as human skin's barrier function makes it resistant to enzymatic digestion and macromolecule penetration. Thus, we applied Deep-STARmap to assess more comprehensively tumor organization and tumor–immune cell interactions in cSCC.

We curated a targeted list of 254 genes (Supplementary Table 8) from previously published scRNA-seq studies of healthy skin and skin cancers, including markers for common skin and immune cell types[71–74]. Deep-STARmap was performed on a 60-µm-thick section of human cSCC obtained from Mohs micrographic surgery (MMS), a sample that included both cSCC tumor and adjacent healthy skin (Extended Data Fig. 10a). Following cell segmentation in 3D, data processing and integration with a published cSCC scRNA-seq dataset[72], we conducted cell typing and visualized cell clusters on the Uniform Manifold Approximation and Projection (UMAP) space based on single-cell RNA expression (Fig. 4a). Nine cell types were identified using known marker genes: keratinocytes, tumor-specific keratinocytes (TSKs), fibroblasts, endothelial cells, B cells, Langerhans cells (LCs), macrophages/dendritic cells (DCs), cytotoxic T cells and regulatory T cells/exhausted T cells (Fig. 4a,b). Deep-STARmap enabled dissection of tumor spatial organization at single-cell resolution. Consistent with histologic tumor spatial patterns noted at the time of MMS, TSKs in this sample were primarily localized to the center of the tissue, whereas nontumor keratinocytes were localized to healthy skin at the sample periphery (Fig. 4c). We performed Deep-STARmap on a second tissue slice from the same patient and confirmed that both the cell typing and expression profiles were highly consistent between the two sections (Extended Data Fig. 10b,c).

Mapping spatial patterns of cell type adjacency in human cSCC

To characterize potential cell–cell interactions, we generated a mesh graph via Delaunay triangulation of cells and computed a near-range cell–cell adjacency matrix based on the normalized number of edges between cell type pairs, as previously described[51,75]. This approach enabled the identification of nearest-neighbor relationships and quantification of cell-type-specific adjacency patterns. A heat map of cell type frequencies among first-tier neighbors revealed clear patterns of cell–cell adjacency (Fig. 4d). The same analysis was performed on a thin 15-µm section of the cSCC sample taken within the same 3D volume (Extended Data Fig. 10d). As expected, more connected

https://doi.org/10.1038/s41592-025-02867-0

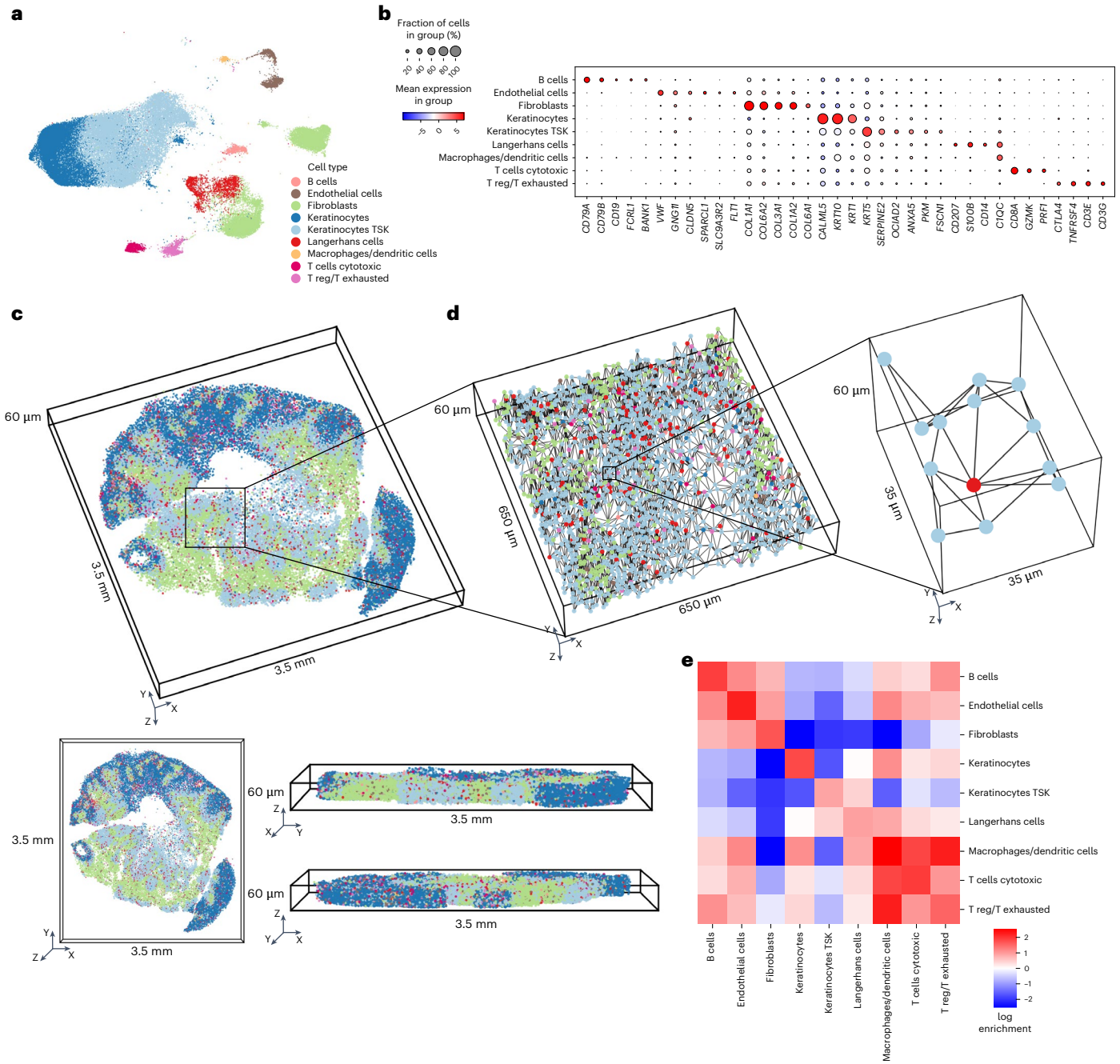

Fig. 4 | Mapping cell–cell adjacency in human cSCC. a, UMAP plot visualization of transcriptional profiles of 51,471 cells, integrated using Harmony with a published cSCC scRNA-seq dataset. Cells are color-coded according to their cell-type identity. **b**, Dot plot illustrating the top differentially expressed marker genes for each major cluster. The color scale represents the $\log_2$ fold change in gene expression compared to the mean gene expression values across all cells. The dot size indicates the percentage of cells expressing the genes within each major cell type. **c**, 3D molecular cell-type maps generated from Deep-STARmap, using the same color coding as in **a**. **d**, Zoomed-in view of the proximity between LCs and TSKs within a mesh graph of physically neighboring cells. Each cell is depicted as a spot colored according to its main cell type, with physically neighboring cells connected by edges. **e**, 3D cell–cell adjacency quantified by log enrichment, calculated as the logarithm of the ratio of observed adjacency frequency to the mean adjacency frequency from 1,000 permutations.

neighbors per cell were detected in thick tissue (mean of 14.3 connected cells) compared to thin tissue (mean of 6.0 connected cells) (Extended Data Fig. 10e,f). This difference arises because projecting 3D cellular architecture onto a 2D plane results in the loss of *z*-dimensional information. Additionally, 3D Delaunay triangulation provides a more comprehensive representation of spatial adjacency by incorporating volumetric context, capturing a greater number of direct cellular interactions compared to 2D analysis.

Across the cSCC sample, cells were often detected in close proximity with cells of the same type. Physical proximity may reflect proliferation or potential interactions between adjacent cells. Of note, TSKs were only found in close proximity to two cell types: other TSKs and LCs, which could be consistent with communication between neighboring TSKs and LCs (Fig. 4d,e). LCs are the major resident antigen-presenting cells of the skin and are known to interact with keratinocytes via E-cadherin. LCs have been reported to encounter cSCC cells before other DC subtypes[76] and stimulate cytotoxic $CD8^+$ T cells and natural killer cells more efficiently than other DC subsets[77]. In our cSCC sample, LCs are adjacent to T cells and TSKs, but not normal keratinocytes outside the tumor, suggesting tumor-specific immune

responses (Fig. 4e). Taken together, our Deep-STARmap cSCC data identified a disease-relevant potential interaction between TSKs and LCs with more accurate and comprehensive cell–cell distance measurements and enrichment analysis compared to 2D analysis.

Discussion

In this study, we present Deep-STARmap and Deep-RIBOmap as imaging platforms for in situ transcriptomic and translatomic sequencing within intact tissue blocks. To enable robust performance and scalability over existing approaches, we introduced strategies for thick-tissue RNA imaging, including scalable probe synthesis, efficient probe anchoring and robust cDNA crosslinking. These technological developments are pivotal for scaling up 3D in situ transcriptomic and translatomic profiling to encompass thousands of genes and across larger tissue regions. This scalability facilitates the integration of molecular characterizations with morphology mapping in neuroscience within thick tissue blocks. We demonstrated that Deep-STARmap and Deep-RIBOmap could successfully profile the transcription and translation of over 1,000 genes within intact 150-µm mouse brain tissue sections, substantially expanding the readouts from larger cell populations. Incorporating combinatorial fluorescence labeling using the Tetbow system allowed high-throughput in situ co-profiling of spatial transcriptomics and single-neuron morphology in thick tissue blocks, enabling multimodal mapping on a volumetric scale previously unattainable. For example, our platform is potentially compatible with MAPseq[16] and BARseq[17] to uncover the organizing principles of neuronal circuitry in thick tissue blocks. Moreover, our platform can be further applied to decode the spatial transcriptomics and translatomics of specific neurons with activity dynamics being collected by live imaging.

We define 200 µm as the practical limit for Deep-STARmap and Deep-RIBOmap based on quantitative depth-dependent performance analyses. Within the first 200 µm, total RNA reads and average reads per cell remain stable, ensuring robust transcript detection. Beyond this depth, RNA counts progressively decline, reaching ~75% at 220 µm and ~60% at 250 µm. Imaging constraints, including the numerical aperture and working distance of the objective lens, further limit performance beyond 300 µm. These findings establish 200 µm as the threshold for reliable spatial transcriptomic measurements in thick tissue samples.

Our platform can also be generalized to study various heterogeneous cell populations in diverse tissues. We demonstrated that our 3D in situ profiling platform is adaptable for profiling difficult-to-digest human skin cancer samples, providing more accurate and quantitative measurements of tumor–immune spatial patterns. For these samples, we adjusted the section thickness to 60 µm to accommodate the presence of dense structural proteins such as keratin and collagen, which complicate proteinase K digestion. Furthermore, we anticipate that our 3D in situ profiling platform will be highly useful for studying human organoid cultures, which are extensively used to replicate in vivo 3D organ development from thin embryonic germ layers during organogenesis[78]. These organoids, typically measuring hundreds of micrometers, necessitate in situ profiling in both healthy and diseased states to advance our understanding of human tissue development, pathology and therapeutic responses.

Nonetheless, it is important to acknowledge certain limitations of our method, particularly its partial capture of large neuronal structures. As documented in resources such as the Allen Brain Atlas, many neuronal types, including those with extensive processes, often exceed 200 µm in size. Consequently, their complete morphological features may not be fully represented within the 150-µm section thickness shown in our demonstration. Additionally, while *z*-compensation methods maintain imaging quality at this depth, light scattering poses a challenge for imaging beyond 150 µm in uncleared tissues. Multiphoton microscopy might overcome some of these depth limitations. RCA imposes spatial constraints on the number of amplicons per cell that can be detected, leading to signal saturation in cells with high RNA content. As a result, Deep-STARmap and Deep-RIBOmap capture the relative percentage rather than absolute numbers of each transcript.

In summary, 3D in situ spatial transcriptomics and translatomics, exemplified by Deep-STARmap and Deep-RIBOmap, offer a robust methodology for integrating molecular data with high-resolution cellular imaging. This comprehensive approach allows for detailed analysis of anatomical and functional dynamics within tissues. Such techniques are poised to substantially enhance our understanding of the underlying mechanisms of tissue functionality and pathology, thereby facilitating deeper scientific exploration and potential therapeutic innovations.

Online content

Any methods, additional references, Nature Portfolio reporting summaries, source data, extended data, supplementary information, acknowledgements, peer review information; details of author contributions and competing interests; and statements of data and code availability are available at https://doi.org/10.1038/s41592-025-02867-0.

References

1. Tabula Sapiens Consortium et al. The Tabula Sapiens: a multiple-organ, single-cell transcriptomic atlas of humans. *Science* **376**, eabl4896 (2022).
2. Elmentaite, R., Domínguez Conde, C., Yang, L. & Teichmann, S. A. Single-cell atlases: shared and tissue-specific cell types across human organs. *Nat. Rev. Genet.* **23**, 395–410 (2022).
3. Hwang, B., Lee, J. H. & Bang, D. Single-cell RNA sequencing technologies and bioinformatics pipelines. *Exp. Mol. Med.* **50**, 1–14 (2018).
4. Baysoy, A., Bai, Z., Satija, R. & Fan, R. The technological landscape and applications of single-cell multi-omics. *Nat. Rev. Mol. Cell Biol.* **24**, 695–713 (2023).
5. Brar, G. A. & Weissman, J. S. Ribosome profiling reveals the what, when, where and how of protein synthesis. *Nat. Rev. Mol. Cell Biol.* **16**, 651–664 (2015).
6. Ingolia, N. T. Ribosome profiling: new views of translation, from single codons to genome scale. *Nat. Rev. Genet.* **15**, 205–213 (2014).
7. Vandereyken, K., Sifrim, A., Thienpont, B. & Voet, T. Methods and applications for single-cell and spatial multi-omics. *Nat. Rev. Genet.* **24**, 494–515 (2023).
8. Zhuang, X. Spatially resolved single-cell genomics and transcriptomics by imaging. *Nat. Methods* **18**, 18–22 (2021).
9. Lein, E., Borm, L. E. & Linnarsson, S. The promise of spatial transcriptomics for neuroscience in the era of molecular cell typing. *Science* **358**, 64–69 (2017).
10. Liao, J., Lu, X., Shao, X., Zhu, L. & Fan, X. Uncovering an organ's molecular architecture at single-cell resolution by spatially resolved transcriptomics. *Trends Biotechnol.* **39**, 43–58 (2021).
11. Ren, J., Luo, S., Shi, H. & Wang, X. Spatial omics advances for in situ RNA biology. *Mol. Cell* **84**, 3737–3757 (2024).
12. Richardson, D. S. & Lichtman, J. W. Clarifying tissue clearing. *Cell* **162**, 246–257 (2015).
13. Ueda, H. R. et al. Tissue clearing and its applications in neuroscience. *Nat. Rev. Neurosci.* **21**, 61–79 (2020).
14. Livet, J. et al. Transgenic strategies for combinatorial expression of fluorescent proteins in the nervous system. *Nature* **450**, 56–62 (2007).
15. Sakaguchi, R., Leiwe, M. N. & Imai, T. Bright multicolor labeling of neuronal circuits with fluorescent proteins and chemical tags. *eLife* https://doi.org/10.7554/elife.40350 (2018).
16. Kebschull, J. M. et al. High-throughput mapping of single-neuron projections by sequencing of barcoded RNA. *Neuron* **91**, 975–987 (2016).

17. Chen, X. et al. High-throughput mapping of long-range neuronal projection using in situ sequencing. *Cell* **179**, 772–786.e19 (2019).
18. Jun, J. J. et al. Fully integrated silicon probes for high-density recording of neural activity. *Nature* **551**, 232–236 (2017).
19. Manz, K. M., Siemann, J. K., McMahon, D. G. & Grueter, B. A. Patch-clamp and multi-electrode array electrophysiological analysis in acute mouse brain slices. *STAR Protoc.* **2**, 100442 (2021).
20. Li, Q. et al. Multimodal charting of molecular and functional cell states via in situ electro-sequencing. *Cell* **186**, 2002–2017.e21 (2023).
21. Gouwens, N. W. et al. Integrated morphoelectric and transcriptomic classification of cortical GABAergic cells. *Cell* **183**, 935–953.e19 (2020).
22. Fuzik, J. et al. Integration of electrophysiological recordings with single-cell RNA-seq data identifies neuronal subtypes. *Nat. Biotechnol.* **34**, 175–183 (2016).
23. Cadwell, C. R. et al. Electrophysiological, transcriptomic and morphologic profiling of single neurons using Patch-seq. *Nat. Biotechnol.* **34**, 199–203 (2016).
24. Xu, S. et al. Behavioral state coding by molecularly defined paraventricular hypothalamic cell type ensembles. *Science* https://doi.org/10.1126/science.abb2494 (2020).
25. Yang, W. & Yuste, R. In vivo imaging of neural activity. *Nat. Methods* **14**, 349–359 (2017).
26. Bugeon, S. et al. Publisher correction: a transcriptomic axis predicts state modulation of cortical interneurons. *Nature* **609**, E10 (2022).
27. Almagro, J., Messal, H. A., Zaw Thin, M., van Rheenen, J. & Behrens, A. Tissue clearing to examine tumour complexity in three dimensions. *Nat. Rev. Cancer* **21**, 718–730 (2021).
28. Fang, R. et al. Three-dimensional single-cell transcriptome imaging of thick tissues. *eLife* https://doi.org/10.7554/eLife.90029 (2023).
29. Wang, Y. et al. EASI-FISH for thick tissue defines lateral hypothalamus spatio-molecular organization. *Cell* **184**, 6361–6377.e24 (2021).
30. Gandin, V. et al. Deep-tissue transcriptomics and subcellular imaging at high spatial resolution. *Science* **388**, eadq2084 (2025).
31. Wang, X. et al. Three-dimensional intact-tissue sequencing of single-cell transcriptional states. *Science* https://doi.org/10.1126/science.aat5691 (2018).
32. Chung, K. et al. Structural and molecular interrogation of intact biological systems. *Nature* **497**, 332–337 (2013).
33. Kanatani, S. et al. Whole-brain spatial transcriptional analysis at cellular resolution. *Science* **386**, 907–915 (2024).
34. Clarke, D. N., Formery, L. & Lowe, C. J. See-Star: a versatile hydrogel-based protocol for clearing large, opaque and calcified marine invertebrates. *Evodevo* **15**, 8 (2024).
35. Choi, H. M. T. et al. Programmable in situ amplification for multiplexed imaging of mRNA expression. *Nat. Biotechnol.* **28**, 1208–1212 (2010).
36. Choi, H. M. T., Beck, V. A. & Pierce, N. A. Next-generation in situ hybridization chain reaction: higher gain, lower cost, greater durability. *ACS Nano.* https://doi.org/10.1021/nn405717p (2014).
37. Shah, S. et al. Single-molecule RNA detection at depth by hybridization chain reaction and tissue hydrogel embedding and clearing. *Development* **143**, 2862–2867 (2016).
38. Choi, H. M. T. et al. Mapping a multiplexed zoo of mRNA expression. *Development* **143**, 3632–3637 (2016).
39. Choi, H. M. T. et al. Third-generation hybridization chain reaction: multiplexed, quantitative, sensitive, versatile, robust. *Development* https://doi.org/10.1242/dev.165753 (2018).
40. Yang, B. et al. Single-cell phenotyping within transparent intact tissue through whole-body clearing. *Cell* **158**, 945–958 (2014).
41. Sylwestrak, E. L., Rajasethupathy, P., Wright, M. A., Jaffe, A. & Deisseroth, K. Multiplexed intact-tissue transcriptional analysis at cellular resolution. *Cell* **164**, 792–804 (2016).
42. Yoshimura, Y. & Fujimoto, K. Ultrafast reversible photo-cross-linking reaction: toward in situ DNA manipulation. *Org. Lett.* **10**, 3227–3230 (2008).
43. Yoshimura, Y., Ohtake, T., Okada, H. & Fujimoto, K. A new approach for reversible RNA photocrosslinking reaction: application to sequence-specific RNA selection. *ChemBioChem* **10**, 1473–1476 (2009).
44. Fujimoto, K., Konishi-Hiratsuka, K., Sakamoto, T. & Yoshimura, Y. Site-specific cytosine to uracil transition by using reversible DNA photo-crosslinking. *ChemBioChem* **11**, 1661–1664 (2010).
45. Chen, F. et al. Nanoscale imaging of RNA with expansion microscopy. *Nat. Methods* **13**, 679–684 (2016).
46. Chen, K. H., Boettiger, A. N., Moffitt, J. R., Wang, S. & Zhuang, X. RNA imaging. Spatially resolved, highly multiplexed RNA profiling in single cells. *Science* **348**, aaa6090 (2015).
47. Zeng, H. et al. Spatially resolved single-cell translatomics at molecular resolution. *Science* **380**, eadd3067 (2023).
48. Zeisel, A. et al. Molecular architecture of the mouse nervous system. *Cell* **174**, 999–1014.e22 (2018).
49. Saunders, A. et al. Molecular diversity and specializations among the cells of the adult mouse brain. *Cell* **174**, 1015–1030.e16 (2018).
50. Tasic, B. et al. Shared and distinct transcriptomic cell types across neocortical areas. *Nature* **563**, 72–78 (2018).
51. Shi, H. et al. Spatial atlas of the mouse central nervous system at molecular resolution. *Nature* **622**, 552–561 (2023).
52. He, Y. et al. Towards a universal spatial molecular atlas of the mouse brain. Preprint at *bioRxiv* https://doi.org/10.1101/2024.05.27.594872 (2024).
53. Korsunsky, I. et al. Fast, sensitive and accurate integration of single-cell data with Harmony. *Nat. Methods* **16**, 1289–1296 (2019).
54. Dong, H. W. & The Allen Institute for Brain Science. *The Allen Reference Atlas, (Book + CD-ROM): A Digital Color Brain Atlas of the C57BL/6J Male Mouse* (Wiley, 2008).
55. Legland, D., Arganda-Carreras, I. & Andrey, P. MorphoLibJ: integrated library and plugins for mathematical morphology with ImageJ. *Bioinformatics* **32**, 3532–3534 (2016).
56. Amitai, Y. et al. The spatial dimensions of electrically coupled networks of interneurons in the neocortex. *J. Neurosci.* **22**, 4142–4152 (2002).
57. Ebina, T. et al. 3D clustering of GABAergic neurons enhances inhibitory actions on excitatory neurons in the mouse visual cortex. *Cell Rep.* **9**, 1896–1907 (2014).
58. Gibson, J. R., Beierlein, M. & Connors, B. W. Two networks of electrically coupled inhibitory neurons in neocortex. *Nature* **402**, 75–79 (1999).
59. Xu, C. S. et al. Enhanced FIB-SEM systems for large-volume 3D imaging. *eLife* https://doi.org/10.7554/elife.25916 (2017).
60. Scheffer, L. K. et al. A connectome and analysis of the adult central brain. *eLife* https://doi.org/10.7554/elife.57443 (2020).
61. Cai, D., Cohen, K. B., Luo, T., Lichtman, J. W. & Sanes, J. R. Improved tools for the Brainbow toolbox. *Nat. Methods* **10**, 540–547 (2013).
62. Chan, K. Y. et al. Engineered AAVs for efficient noninvasive gene delivery to the central and peripheral nervous systems. *Nat. Neurosci.* **20**, 1172–1179 (2017).
63. Spruston, N. Pyramidal neurons: dendritic structure and synaptic integration. *Nat. Rev. Neurosci.* **9**, 206–221 (2008).
64. Jiang, S. et al. Anatomically revealed morphological patterns of pyramidal neurons in layer 5 of the motor cortex. *Sci. Rep.* **10**, 7916 (2020).
65. Zeng, H. What is a cell type and how to define it?. *Cell* **185**, 2739–2755 (2022).

66. Guzman, A. K., Schmults, C. D. & Ruiz, E. S. Squamous cell carcinoma: an update in staging, management, and postoperative surveillance strategies. *Dermatol. Clin.* **41**, 1–11 (2023).
67. Borden, E. S. et al. Neoantigen fitness model predicts lower immune recognition of cutaneous squamous cell carcinomas than actinic keratoses. *Front. Immunol.* **10**, 2799 (2019).
68. Levine, D. E., Karia, P. S. & Schmults, C. D. Outcomes of patients with multiple cutaneous squamous cell carcinomas: a 10-year single-institution cohort study. *JAMA Dermatol.* **151**, 1220–1225 (2015).
69. Gonzalez, J. L. et al. Multiple cutaneous squamous cell carcinoma in immunosuppressed vs immunocompetent patients. *JAMA Dermatol.* **155**, 625–627 (2019).
70. Migden, M. R. et al. PD-1 blockade with cemiplimab in advanced cutaneous squamous-cell carcinoma. *N. Engl. J. Med.* **379**, 341–351 (2018).
71. Joost, S. et al. The molecular anatomy of mouse skin during hair growth and rest. *Cell Stem Cell* **26**, 441–457.e7 (2020).
72. Ji, A. L. et al. Multimodal analysis of composition and spatial architecture in human squamous cell carcinoma. *Cell* **182**, 1661–1662 (2020).
73. Jerby-Arnon, L. et al. A cancer cell program promotes T cell exclusion and resistance to checkpoint blockade. *Cell* **175**, 984–997.e24 (2018).
74. Tirosh, I. et al. Dissecting the multicellular ecosystem of metastatic melanoma by single-cell RNA-seq. *Science* **352**, 189–196 (2016).
75. He, Y. et al. ClusterMap for multi-scale clustering analysis of spatial gene expression. *Nat. Commun.* **12**, 5909 (2021).
76. Fujita, H. et al. Langerhans cells from human cutaneous squamous cell carcinoma induce strong type 1 immunity. *J. Invest. Dermatol.* **132**, 1645–1655 (2012).
77. Klechevsky, E. et al. Functional specializations of human epidermal Langerhans cells and CD14$^+$ dermal dendritic cells. *Immunity* **29**, 497–510 (2008).
78. Calà, G., Sina, B., De Coppi, P., Giobbe, G. G. & Gerli, M. F. M. Primary human organoids models: current progress and key milestones. *Front. Bioeng. Biotechnol.* **11**, 1058970 (2023).

Methods

Animal husbandry

All animal procedures adhered to the care guidelines approved by the Institutional Animal Care and Use Committee of the Broad Institute, under animal protocol no. 0255-08-19. Female C57/BL6 mice aged 6–10 weeks were procured from the Jackson Laboratory (JAX). Mice were housed 4–5 per cage, with food and water in a room with 18–23 °C temperature and 40–60% humidity under a 12-h light–dark cycle.

Human cutaneous squamous cell carcinoma samples

Human cutaneous squamous cell carcinoma tissue was obtained from deidentified discarded hospital specimens approved under the Massachusetts General Hospital Research Committee/institutional review board protocol no. 2013P000093.

Tetbow AAV injections

The AAV plasmids utilized in this study include pAAV-TRE-mTurquoise2-WPRE (Addgene, #104110), pAAV-TRE-EYFP-WPRE (Addgene, #104111), pAAV-TRE-tdTomato-WPRE (Addgene, #104112), and pAAV-ihSyn1-tTA (Addgene, #99120). Tetbow components were packaged into AAV.PHP.eB as previously described[62]. In brief, for each capsid, HEK 293T cells (ATCC CRL-3216) were transfected with a combination of pAAV plasmid and two AAV packaging plasmids (kiCAP-AAV-PHP.eB and pHelper) in a 1:4:2 weight ratio, using polyethyleneimine, with a total of 40 µg of DNA per 150-mm dish. Fluorescence expression, when applicable, was evaluated via microscopy, and the medium was refreshed 20–24 h post-transfection. Viral particles were collected 72 h post-transfection from both cells and medium by centrifugation, forming cell pellets. Cell pellets were then resuspended in a buffer containing 500 mM NaCl, 40 mM Tris, 10 mM $MgCl_2$, pH ~10 and 100 U ml^{-1} of salt-activated nuclease (SAN, 25 U μl^{-1}, Arcticzymes, 70910-202) and incubated at 37 °C for 1.5 h. Following incubation, the cell lysates were subjected to centrifugation at 2,000*g* to remove cellular debris. The viral particles were isolated through a series of iodixanol gradient steps (15%, 25%, 40% and 60%). Viruses were collected from both the 40–60% interface and the 40% iodixanol layer. Concentration of the viral particles and buffer change were achieved using Pierce Protein Concentrators (Thermo Scientific, 88528), and they were subsequently suspended in sterile phosphate-buffered saline (PBS). To quantify viral titers, viral genomes were measured using quantitative PCR (qPCR). Samples were treated with DNase I (Roche Diagnostics, 4716728001) to eliminate non-packaged DNA and subsequently with proteinase K (Roche Diagnostics, 03115828001) to digest the viral capsid, thereby exposing the viral genomes for qPCR quantification. A linearized genome plasmid served as the reference standard. The viral titers for tTA, tdTomato, EYFP and mTurquoise2 were 2.15×10^{13}, 2.31×10^{13}, 3.04×10^{13} and 2.63×10^{13} vg per ml, respectively.

Intravenous administration of the AAV.PHP.eB mixture (1×10^{11} vg tTA, 3.33×10^{11} vg tdTomato, 3.33×10^{11} vg EYFP, 3.33×10^{11} vg mTurquoise2) was performed via injection into the retro-orbital sinus of adult female C57BL/6 mice (8–10 weeks of age). At 28 days post-injection, the mice were anesthetized with isoflurane. Transcardial perfusion was carried out, initially with 50 ml of cold PBS, followed by 50 ml of 4% PFA. The entire brain was then post-fixed in 4% PFA at 4 °C for 3 h. Subsequently, the brain was washed multiple times with PBS and placed in a 30% sucrose solution (in PBS) at 4 °C overnight or until it had sunk. Finally, the brain was embedded in O.C.T. (Fisher, 23-730-571) and frozen in liquid nitrogen and stored at −80 °C. Thick tissue sections were prepared and transferred into pretreated glass-bottom plates.

Chemicals and enzymes

Chemicals and enzymes are listed as name (supplier, cat. no.): 12-well plate, no. 1.5 coverslip, 14-mm Glass Diameter, Uncoated (MatTek, P12G-1.5-14-F); PlusOne Bind-Silane (Sigma, 440159); 16% PFA, EM grade (Electron Microscope Sciences, 15710-S); methanol (Sigma-Aldrich, 34860-1L-R); Tween-20, 10% solution (Teknova, T0710); Triton X-100, 10% solution (Sigma-Aldrich, 93443-100 ML); 10× PBS (Thermo Fisher, 70011044); 1× PBS (Thermo Fisher, 10010049); 20× SSC buffer (Thermo Fisher, 15557044); methacrylic acid *N*-hydroxysuccinimide ester, 98% (Sigma-Aldrich, 730300-1G); acrylamide solution, 40% (Bio-Rad, 161-0140); Bis solution, 2% (Bio-Rad, 161-0142); ammonium persulfate (Sigma-Aldrich, A3678-100G); N,N,N′,N′-tetramethylethylenediamine (Sigma-Aldrich, T9281-50ML); OmniPur SDS, 20% (Calbiochem/Sigma, 7990-200ML); NeuroTrace Fluorescent Nissl Stains, yellow (Molecular Probes/Fisher Scientific, N21480); Cover Glass Circle, 12 mm, #2, 1oz/BX (Electron Microscopy Sciences, 72226-01); Gel Slick Solution (Lonza, 50640); Formamide, Deionized (Sigma-Aldrich, 4650-500ML); Antarctic phosphatase reaction buffer (New England Biolabs, B0289S); Antarctic phosphatase (New England Biolabs, M0289L); BSA (New England Biolabs, B9200S); glycine (Sigma-Aldrich, 50046-250G); ribonucleoside vanadyl complex (New England Biolabs, S1402S); dimethylsulfoxide, anhydrous (Invitrogen/Thermo Fisher, D12345); DNase/RNase-free distilled water (Invitrogen/Thermo Fisher, 10977023); 4′,6-diamidino-2-phenylindole (DAPI) (Thermo Fisher, 62248); acetic acid (Sigma-Aldrich, A6283-100ML); poly-D-lysine (Thermo Fisher, A3890401); dNTP mix (Thermo Fisher, 18427089); 5-(3-aminoallyl)-dUTP (Invitrogen, AM8439); BSPEG9 (Thermo Fisher, 21582); Proteinase K Solution (Invitrogen, 25530049); SUPERase·In RNase Inhibitor (Thermo Fisher, AM2696); T4 DNA Ligase (Thermo Fisher, EL0012); Phi29 DNA Polymerase (Thermo Fisher, EP0094); and yeast tRNA (Thermo Fisher, AM7119).

Deep-STARmap and Deep-RIBOmap probe design

Deep-STARmap and Deep-RIBOmap padlock and primer probes were developed based on the methodologies outlined by Wang et al. and Zeng et al., with specific modifications[31,47]. Each Deep-STARmap and Deep-RIBOmap primer incorporated a 'flanking linker sequence' (CCTACCAGTACGACGTATTTAGCAA) at the 5′ end to enable hybridization with an Acrydite-modified oligonucleotide. The Deep-RIBOmap additionally required a splint probe, composed of three segments: a 25-nt sequence at the 5′ end complementary to the 18S ribosomal RNA (rRNA), a 50-nt deoxyadenosine nucleotides (dA), and a 12-nucleotide padlock template at the 3′ end. To prevent the 3′ terminus of the splint probes from serving as an RCA primer, a 3′ Inverted dT modification was included. The same 5′ linker sequence was also added to the splint.

Adaptor and primer pretreatment

The ^{CNV}K-containing adaptor ([5Acryd]GCTA[^{cnv}K]ATACGTCGTACTGGTAGG[Inv-dT], ordered from Gene Link with PAGE purification) undergoes rapid photo crosslinking to the complementary strand through an adjacent pyrimidine base upon UV irradiation. The irradiation process was conducted using the Boekel UV Crosslinker (234100) equipped with 368 nm-wavelength bulbs (Boekel part no. 920-0307) for 10–30 min. The adaptor to primer was maintained at a molar ratio of 5:1 in water or IDTE buffer.

Deep-STARmap and Deep-RIBOmap protocol

Glass-bottom 12-well plates (Mattek, P12G-1.5-14-F) were treated with oxygen plasma using the Anatech Barrel Plasma System at 100 W and 40% O_2 for 5 min. The plates were immersed in a 1% methacryloxypropyltrimethoxysilane (Bind-Silane) solution for 60 min at room temperature. The plates then underwent three consecutive ethanol washes and were allowed to air dry. Subsequently, a 0.1 mg ml^{-1} poly-D-lysine solution was applied to the plates for 1 h, followed by three rinses with distilled water.

Deep-STARmap and Deep-RIBOmap samples were cryosectioned at 150 µm for 1,017-gene experiments; human cSCC samples were sectioned at 60 µm. While cryosectioning was used in this study (allowing −80 °C storage), both protocols were compatible with vibratome sections.

Tissue slices were transferred to pretreated glass-bottom 12-well plates and permeabilized using 1 ml of prechilled methanol at −20 °C for 1 h. Samples were then washed with 500 µl PBSTR (0.1% Triton X-100, 0.1 U µl^{-1} SUPERase·In in PBS) for 30 min, quenched with 500 µl of 1 mg ml^{-1} yeast tRNA and 100 mM glycine in PBSTR at room temperature for 30 min, and washed again with PBSTR. Subsequently, hybridization buffers were prepared. The base composition of the hybridization buffer included 2× SSC, 10% formamide, 1% Triton X-100, 20 mM RVC, 0.1 mg ml^{-1} yeast tRNA, 0.1 U µl^{-1} SUPERase·In and 0.2% SDS. Deep-STARmap samples received 5 nM each of pooled padlock and pretreated primers; Deep-RIBOmap samples additionally included 100 nM pretreated splint probe. The samples were incubated in 300 µl of hybridization buffer in a 40 °C humidified oven with gentle shaking for 36 h. After incubation, the samples were washed for 30 min with PBSTR, followed by a 30-min wash in high salt buffer (4× SSC in PBSTR) at 37 °C. Finally, the samples were washed once more with PBSTR at 37 °C.

To cast the tissue–hydrogel hybrid, the samples were first incubated with monomer buffer (4% acrylamide, 0.2% bis-acrylamide and 2× SSC) supplemented with 0.2% TEMED and 0.25% VA-044 at 4 °C for 60 min. Following incubation, the buffer was aspirated and 55 µl of a polymerization mixture (0.2% TEMED, 0.2% ammonium persulfate and 0.25% VA-044 in monomer buffer) was added to the center of the sample and immediately covered with a Gel Slick-coated coverslip. Polymerization was carried out at 40 °C in a N_2 oven for 90 min. Subsequently, the sample was washed with PBSTR three times for 15 min each. For Tetbow mice samples, the tissue was stained with DAPI for 3 h and then immersed in washing and imaging buffer (10% formamide in 2× SSC buffer) containing 0.1 U µl^{-1} SUPERase·In RNase inhibitor. Confocal images of tdTomato, EYFP, mTurquoise2 and DAPI were acquired using an inverted confocal microscope, Leica TCS SP8 (v.3.5.5.19976), equipped with a 405 nm and 442 nm diode, a white light laser, HyD detectors and a ×25 water-immersion objective (NA 0.95). The voxel size for imaging was 0.32 × 0.32 × 0.70 µm. Excitation wavelengths were 405 nm (DAPI), 442 nm (mTurquoise2), 506 nm (EYFP) and 550 nm (tdTomato).

The tissue–gel hybrids were then digested with 1 ml Proteinase K mixture (0.4 mg ml^{-1} Proteinase K in 2× SSC and 1% SDS) at 37 °C overnight, then washed in PBSTR three times for 30 min each. The sample was incubated in ligation mixture (0.25 U µl^{-1} T4 DNA ligase, 1:100 BSA and 0.2 U µl^{-1} SUPERase·In RNase inhibitor) at room temperature overnight with gentle shaking and then washed with PBSTR three times for 30 min each. Then the sample was incubated with 400 µl RCA mixture (0.5 U µl^{-1} Phi29 DNA polymerase, 250 µM dNTP, 20 µM 5-(3-aminoallyl)-dUTP, 1:100 BSA and 0.2 U µl^{-1} of SUPERase·In RNase inhibitor in 1× Phi29 buffer) at 4 °C for 60 min for equilibrium before incubating at 30 °C for 8–14 h for amplification and washed with PBST three times for 30 min each. The samples were treated with 20 mM methacrylic acid *N*-hydroxysuccinimide ester in 100 mM sodium bicarbonate buffer for 4 h to overnight at room temperature. Following the same procedures for casting the tissue–hydrogel hybrid, cDNA amplicons were re-embedded with 2% acrylamide, 0.05% bis-acrylamide to enable cDNA amplicon crosslinking in the tissue–hydrogel setting. Samples were stored in PBST or wash and imaging buffer at 4 °C.

Before SEDAL sequencing, the samples were treated with the dephosphorylation mixture (0.25 U µl^{-1} Antarctic phosphatase and 1× BSA in 1× Antarctic phosphatase buffer) at 37 °C for 4 h and washed by PBST three times for 30 min each. Each sequencing cycle began with treating the sample three times, 15 min each, with the stripping buffer (60% formamide and 0.1% Triton X-100 in water) at room temperature, followed by washing with PBST three times for 15 min each. Then the samples were incubated with 300 µl of sequencing-by-ligation mixture (0.2 U µl^{-1} T4 DNA ligase, 1× BSA, 10 µM reading probe and 5 µM fluorescent decoding oligonucleotides in 1× T4 DNA ligase buffer) at room temperature overnight, followed by rinsing with washing and imaging buffer three times for 10 min each before imaging. Imaging was performed using the same Leica TCS SP8 with voxel dimensions of 0.32 × 0.32 × 0.70 µm. Alexa Fluor 488, 546, 594 and 647 were used for signal detection. DAPI staining was carried out 3 h before the first cycle and imaged using the 405 nm channel. A total of six imaging cycles were completed to decode 1,017 genes.

Data processing for Deep-STARmap and Deep-RIBOmap

Deconvolution. Image deconvolution was achieved with Huygens Essential v.23.4.0 (Scientific Volume Imaging, http://svi.nl). We applied the classic maximum likelihood estimation method with a signal-to-noise ratio of ten and ten iterations.

Image registration, spot calling and barcode filtering. For image registration, spot calling and barcode filtering, we utilized our custom software package, Starfinder (https://github.com/wanglab-broad/starfinder). This software corrects chromatic aberrations, enhances signals, registers images and extracts positive reads (amplicons). Adjustments were made to accommodate the large datasets generated by thick tissue profiling. In short, image clarity is enhanced by intensity normalization and histogram equalization where images in the first sequencing round are used as reference. To ensure accurate and reliable identification of each cDNA amplicon's barcode, we utilized a two-step registration process. First, we conducted a global registration using 3D fast Fourier transform. Next, we applied a nonrigid registration using MATLAB v.2023b's 'imregdemons' function. This method adjusts for any shifts and distortions between imaging sessions. As the amplicon size is larger than amplicons in thin tissue, we applied a medium filter with 'medfilt2' function in a 3 × 3 or 2 × 2 (depending on the average amplicon size) neighborhood around the corresponding pixel in the input image. Dots with intensity at their centroids less than the threshold were removed. The process of identifying individual amplicons in 3D was carried out using the 'imregionalmax' function in MATLAB to find local maxima within the images from the first sequencing round. The dominant color for each amplicon across all rounds of sequencing was then determined by estimating the amplicon size and integrating the voxel volume intensity in each channel. Each dot's color composition was represented by an L2-normalized vector with four elements, and dots showing multiple maximum values within this vector were excluded. Initial filtering of dots was based on quality scores, which were computed as the average of −log(color vector value in the dominant channel) across all sequencing rounds. Subsequently, the barcode codebook was translated into color space, following the expected color sequence of the two-base encoded barcode DNA sequence. Only dots that met the quality threshold and had a matching barcode sequence in the codebook were retained, with all others discarded. The 3D physical locations and gene identities of these filtered dots were then preserved for subsequent analysis.

3D segmentation. 3D image segmentation was performed based on the DAPI staining image and the composite image containing amplicon channels to create reference segmentations as previously described with minor adjustments[47,51,79]. Unlike thin tissue analysis, where images are stitched before segmentation, this approach is impractical for thick tissue profiling because the stitched files are too large for effective segmentation. Therefore, segmentation was performed on each field of view (FOV) individually and the identified amplicons were stitched afterward. For each FOV, images targeting different cellular compartments were first processed using a median filter and then binarized with an automatically determined threshold in Fiji. Distance Transformed Watershed 3D was subsequently applied to generate a 3D segmentation mask for each cellular region. Connected components (objects) with fewer than 500 voxels were removed from the binary image. Finally, the images were dilated using a disk structure element with a radius of 10.

Reads assignment and stitching. Filtered amplicons overlapping each segmented cell region in 3D were assigned to their respective regions to compute a per-cell gene expression matrix. The TileConfiguration file generated from Fiji grid stitching was then used to merge detected amplicon signals from each FOV, ensuring the removal of duplicated cells and associated reads. Further strategies to exclude low-quality cells were applied as previously described in thin tissue analysis[31,47,51]. For Deep-STARmap in mouse brain samples, the average number of detected reads per cell is 112.2 ± 78.9, whereas for Deep-RIBOmap in mouse brain samples, the average is 84.0 ± 59.9.

Cell type classification via FuseMap. Cell type classification was performed using transfer learning with a pretrained FuseMap model, as previously described[52]. This model maps and annotates new query data with cell-type labels based on cell embeddings. In this study, a previously published brain spatial atlas served as the reference for training the FuseMap model, while thick tissue sections were used as the query datasets for annotation.

Harmony integration. To benchmark FuseMap performance, Harmony integration was employed. First, Deep-STARmap data were combined with thin tissue STARmap data[51] after preprocessing, followed by batch correction using the pp.combat function. Harmony integration was then applied to the combined dataset to create a joint principal-component analysis embedding[80]. A k-nearest neighbor (*k*-NN) classifier was trained on the integrated principal-component space using cosine distance as the metric (n_neighbors = 50, n_pcs = 50, min_dist = 0.01, spread = 5). This classifier was used in a label transfer process to annotate each cell based on its neighboring reference cells in the *k*-NN graph. The label transfer was performed for the annotation at the 'Rank4_Refine' level.

GO enrichment analysis

GO enrichment analysis was conducted using the DAVID database (https://davidbioinformatics.nih.gov/)[81,82]. gProfiler (https://biit.cs.ut.ee/gprofiler/gost) was utilized for GO analysis. Enriched GO terms were selected from biological processes and cellular components with false discovery rate < 0.05 for both cell-type-resolved Deep-STARmap and Deep-RIBOmap profiles, as well as for somata-enriched translation genes and processes-enriched translation genes.

Gene clustering

The gene expression ($\log_2$_norm1e4) of the four samples was first averaged across the cell types within each sample, respectively. Subsequently, the average expression values were standardized by calculating the *z*-score within each sample. The standardized vectors were merged and clustered with the Leiden algorithm from Scanpy[83] (v.1.9.3).

Near-range cell–cell adjacency analysis

To quantify spatial interactions between major cell types, we performed near-range cell–cell adjacency analysis as previously described[75,84]. Adjacency between cell types A and B was defined as the number of A–B edges within a one-hop neighborhood on a Delaunay triangulation graph, constructed using Delaunay package from scipy.spatial. This method connects points (in this case, cell centers) to form triangles such that no points are inside the circumcircle of any triangle, ensuring accurate local neighborhood representation. First-order (one-hop) neighbors were defined as cells directly connected by Delaunay edges. Raw counts of A–B edges were normalized against a null distribution generated from 1,000 random spatial shifts.

Morphological reconstructions

3D single-neuron morphologies were reconstructed from image stacks using Imaris (v.9.7.2–10.1.1, Oxford Instruments). Tetbow-labeled dendrites were traced semi-automatically with the filament tracer in autodepth mode, followed by manual curation. Only confidently connected structures were retained. Any processes that could not be definitively linked to the main structure were left unconnected.

From each neuron, 138 quantitative features were extracted—including total filament length, vertex count, branching angles, soma-to-branch distances, bounding box dimensions and spine metrics—capturing both global and local morphology. We then trained a Random Forest classifier using ~70% of the reconstructed neurons across excitatory, SST interneuron and PV interneuron subtypes and evaluated its ability to correctly classify the remaining 30%. The classifier successfully distinguished neuronal subtypes based on their morphological features, with one exception—a single excitatory neuron that exhibited fewer reconstructed branches. This likely reflects inherent challenges in neuronal tracing, particularly in densely packed environments where axonal and dendritic processes may not be fully resolvable. Feature importance analysis revealed Y-coordinate segment positions and vertex count as top contributors to classification. These findings underscore the critical influence of laminar positioning and morphological complexity in subtype discrimination, while also reflecting the challenges of neuronal tracing in densely packed environments.

Reporting summary

Further information on research design is available in the Nature Portfolio Reporting Summary linked to this article.

Data availability

Deep-STARmap and Deep-RIBOmap sequencing datasets of 1,017-gene in mouse brain, Deep-STARmap datasets of 254-gene in human cutaneous squamous cell carcinoma tissue are available in Zenodo at https://doi.org/10.5281/zenodo.16783354 (ref. 85). The mouse brain atlas dataset used is available at https://singlecell.broadinstitute.org/single_cell/study/SCP1830. The cSCC scRNA-seq dataset used is available at the Gene Expression Omnibus under accession code GSE144240.

Code availability

Deep-STARmap and Deep-RIBOmap are implemented based on MATLAB v.R2023b, Python v.3.8 and R v.4.2.1. The data processing tool has been deposited in Zenodo at https://doi.org/10.5281/zenodo.16783354 (ref. 85). Additional information is available at the Wang laboratory website at https://www.wangxiaolab.org/.

References

79. Ren, J. et al. Spatiotemporally resolved transcriptomics reveals the subcellular RNA kinetic landscape. *Nat. Methods* **20**, 695–705 (2023).
80. Huang, D. W., Sherman, B. T. & Lempicki, R. A. Systematic and integrative analysis of large gene lists using DAVID bioinformatics resources. *Nat. Protoc.* **4**, 44–57 (2009).
81. Huang, D. W., Sherman, B. T. & Lempicki, R. A. Bioinformatics enrichment tools: paths toward the comprehensive functional analysis of large gene lists. *Nucleic Acids Res.* **37**, 1–13 (2009).
82. Shannon, P. et al. Cytoscape: a software environment for integrated models of biomolecular interaction networks. *Genome Res.* **13**, 2498–2504 (2003).
83. Wolf, F. A., Angerer, P. & Theis, F. J. SCANPY: large-scale single-cell gene expression data analysis. *Genome Biol.* **19**, 15 (2018).
84. Palla, G. et al. Squidpy: a scalable framework for spatial omics analysis. *Nat. Methods* **19**, 171–178 (2022).
85. Sui, X. et al. Scalable spatial single-cell transcriptomics and translatomics in 3D thick tissue blocks. *Zenodo* https://doi.org/10.5281/zenodo.16783354 (2025).

Acknowledgements

The authors thank the B. E. Deverman laboratory (Stanley Center for Psychiatric Research, Broad Institute) for helping with AAV

packages and V. Neel (Department of Dermatology, Massachusetts General Hospital) for providing patient SCC samples critical to this study. The authors thank H. Shi, A. Roy, F. Kostas and S. Furniss (Broad Institute) for their helpful feedback and comments during manuscript writing. We thank P. Paroutis and the Hospital for Sick Children imaging facility for software access. X.W. gratefully acknowledges support from Edward Scolnick Professorship, gifts from Stanley Center for Psychiatric Research, Escaping Velocity Award, Ono Pharma Breakthrough Science Initiative Award, Merkin Institute Fellowship and National Institutes of Health (NIH) DP2 New Innovator Award (1DP2GM146245) and NIH BRAIN CONNECTS (UM1 NS132173). J.A.L. gratefully acknowledges support from the NIH (T32AR007098-47), Dermatology Foundation (Dermatologist Investigator Research Fellowship and Physician-Scientist Career Development Award), and BroadIgnite. W.X.W. is a Damon Runyon–National Mah Jongg League Fellow, supported by the Damon Runyon Cancer Research Foundation (DRG no. 2512-23). D.L.B. is supported by funding from the Eric and Wendy Schmidt Center at the Broad Institute of MIT and Harvard. J.L. acknowledges the support of NIH/NIDDK 1DP1DK130673. Figures include graphics created in BioRender (https://BioRender.com/ew2lkjv).

Author contributions

X.S. and X.W. conceived the idea and developed Deep-STARmap and Deep-RIBOmap for the study. X.S. carried out experimental work, performed in situ sequencing and conducted computational and data analyses. J.A.L. designed the gene lists for human cSCC, acquired samples and made significant contributions to the analysis of human cSCC. S.L., Y.H. and Z.T. performed data analysis. Z.L. helped with method optimization. Y.Z. helped with AAV packaging and conducted animal work. W.X.W. helped with morphology analysis. D.L.B. conducted prediction of molecular cell type based on neuronal morphology. J.L. provided critical discussions during method development. X.S., J.A.L. and X.W. wrote the manuscript with input from all authors. X.W. supervised the study.

Competing interests

X.W. and X.S. are inventors on pending patent applications related to Deep-STARmap and Deep-RIBOmap. X.W. is a scientific co-founder and consultant of Stellaromics. All other authors declare no competing interests.

Additional information

Extended data is available for this paper at https://doi.org/10.1038/s41592-025-02867-0.

Supplementary information The online version contains supplementary material available at https://doi.org/10.1038/s41592-025-02867-0.

Correspondence and requests for materials should be addressed to Xiao Wang.

Peer review information *Nature Methods* thanks the anonymous reviewers for their contribution to the peer review of this work. Primary Handling Editor: Lei Tang, in collaboration with the *Nature Methods* team.

https://doi.org/10.1038/s41592-025-02867-0

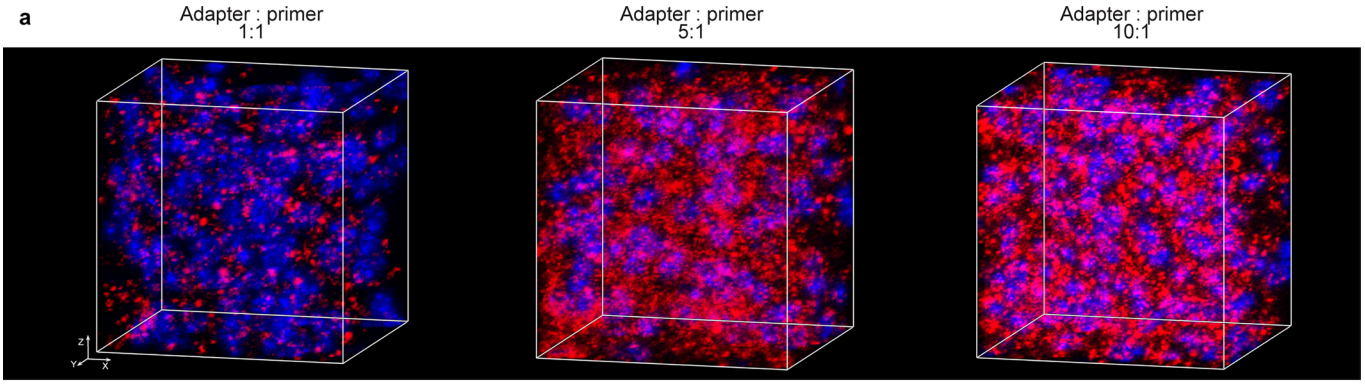

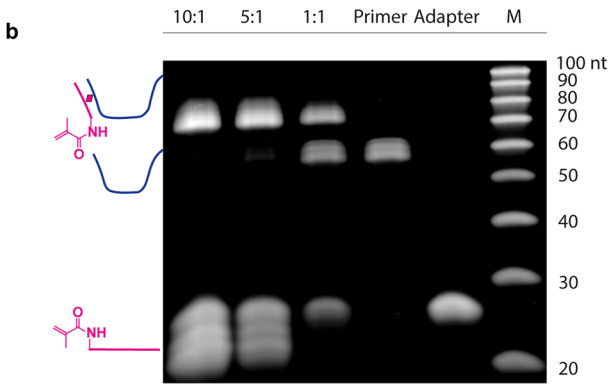

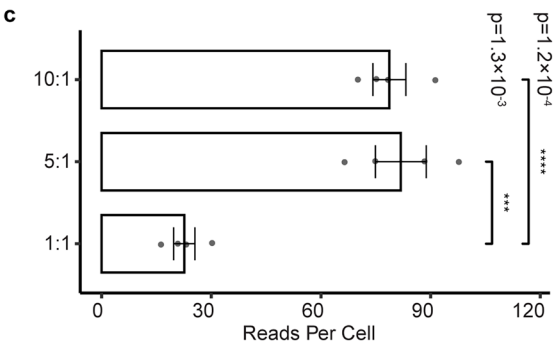

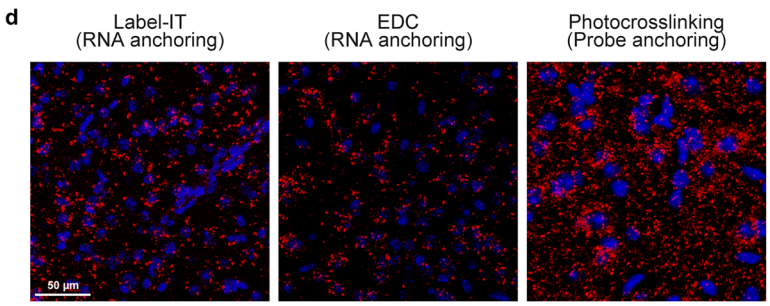

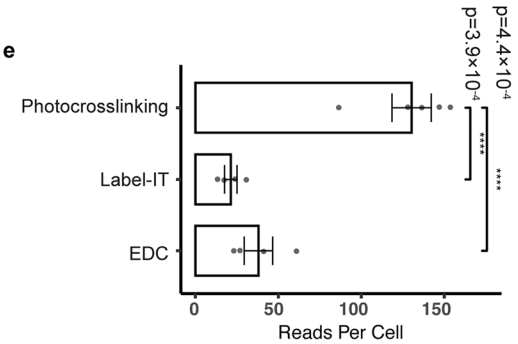

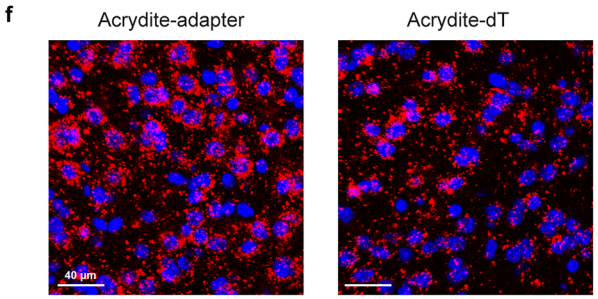

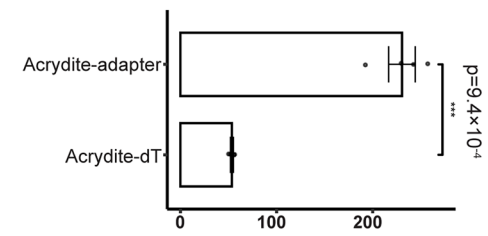

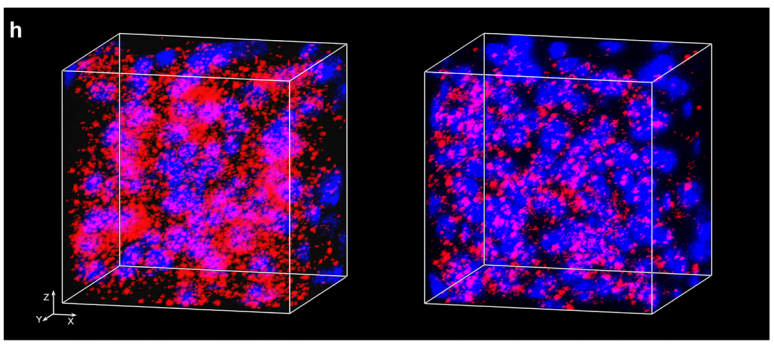

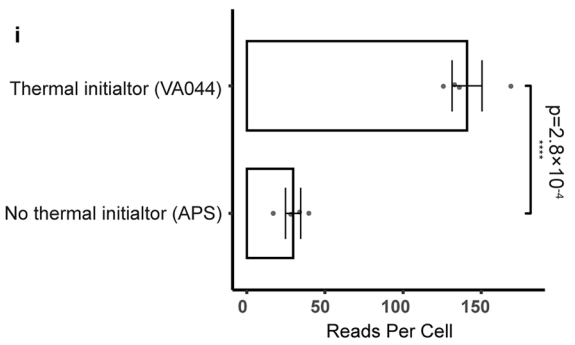

Extended Data Fig. 1 | See next page for caption.

https://doi.org/10.1038/s41592-025-02867-0

Extended Data Fig. 1 | Optimization of probe crosslinking. a, Representative fluorescent imaging illustrating probe anchoring efficiency in a hydrogel matrix with various adaptor-primer ratios. Red: DNA amplicons of brain cell type markers: *Gfap, Snap25, C1qa, Plp1*. Blue: DAPI. Scale bar: 10 µm. *n = 4* technical replicates, each derived from independent cortical regions across four different brain slices. **b**, 15% TBE-Urea gels demonstrating UV crosslinking efficiency with varying adaptor-primer molar ratios. ^{CNV}K- and Acrydite-containing adaptor used for UV crosslinking is [5Acryd]GCTA[cnvK]ATACGTCGTACTGGTAGG[Inv-dT] (24 nt). Primer used is 58 bp ssDNA with a 24 nt flanking liner at the 5′ end. M, Marker: IDT ssDNA 20/100 Ladder. *n = 3* replicates. **c**, Quantification of cell images showing the average amplicon reads per cell (*n = 4* technical replicates, each derived from independent cortical regions across four different brain slices). Two-sided independent *t*-test, ***$P < 0.001$, ****$P < 0.0001$. Data presented as mean ± standard deviation. **d**, Representative fluorescent imaging demonstrating detection efficiency of covalently anchored RNA molecules or probes within the hydrogel in the Deep-STARmap setting. Red: DNA amplicons from 4 cell type markers (Supplementary Table 1). Blue: DAPI. Scale bar: 50 µm. **e**, Quantification of cell images showing the average amplicon reads per cell (n = 4 technical replicates, each derived from independent cortical regions across four different brain slices). Two-sided independent t-test, ****$P < 0.0001$. Data presented as mean ± standard deviation. **f**, Representative fluorescent images of ACTB-gene profiling in tissue sections using Deep-STARmap with an Acrydite-modified adaptor (left) and an Acrydite-modified poly-dT oligo (right). Red: DNA amplicons, blue: DAPI nuclear staining. Scale bar: 40 µm. **g**, Box plot showing the number of reads per cell when using an Acrydite-modified adaptor (top) versus an Acrydite-modified poly-dT oligo (bottom) for anchoring in the Deep-STARmap workflow. *n = 4* technical replicates, each derived from independent cortical regions across four different brain slices. Two-sided independent t-test, ***$P < 0.001$. Data are shown as mean ± standard deviation. **h**, Representative fluorescent imaging demonstrating probe anchoring efficiency with (left) and without (right) the use of the VA-044 thermal initiator in the first round of polymerization. Red: DNA amplicons from 4 cell type markers (Supplementary Table 1). Blue: DAPI. Scale bar: 50 µm. **i**, Quantification of cell images showing the average amplicon reads per cell (n = 4 technical replicates, each derived from independent cortical regions across four different brain slices). Two-sided independent t-test, ****$P < 0.0001$. Data presented as mean ± standard deviation.

https://doi.org/10.1038/s41592-025-02867-0

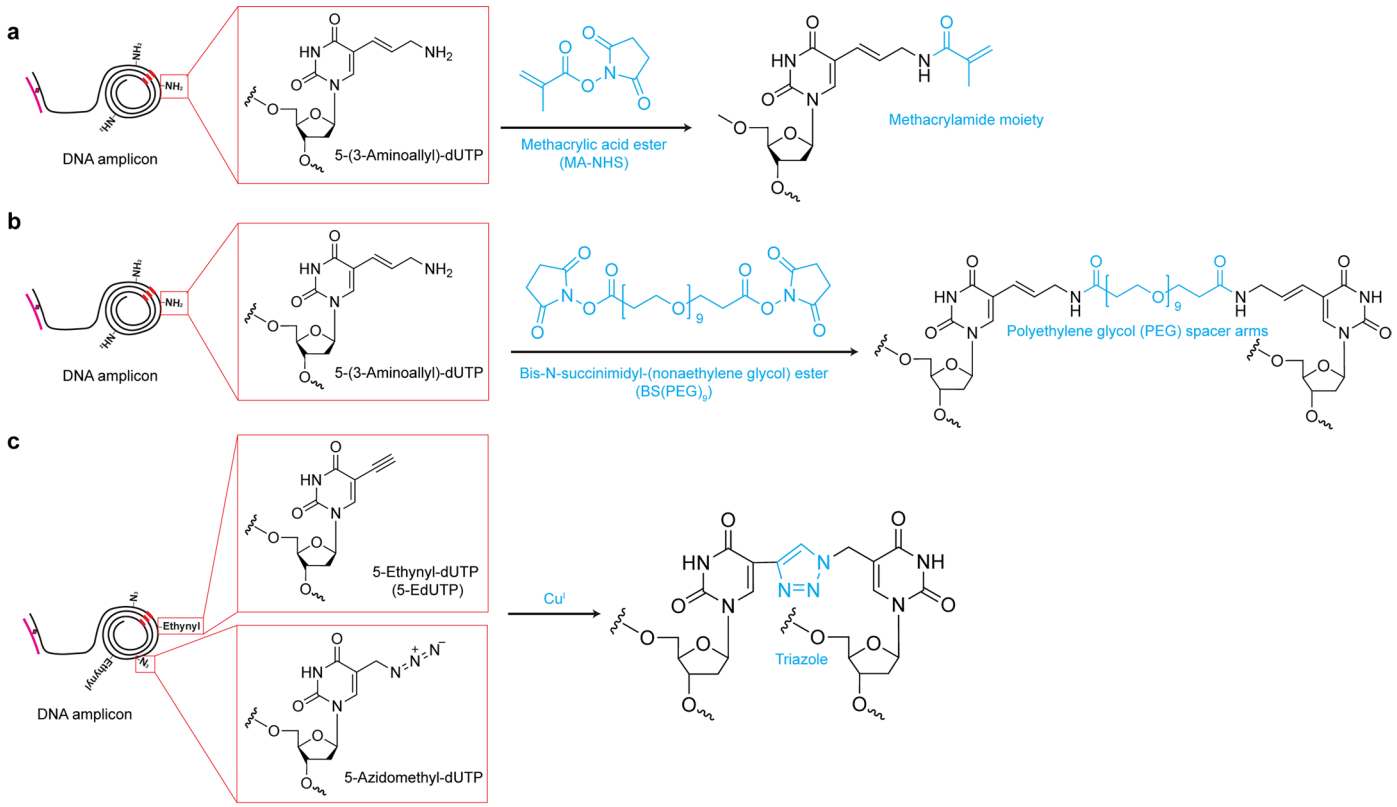

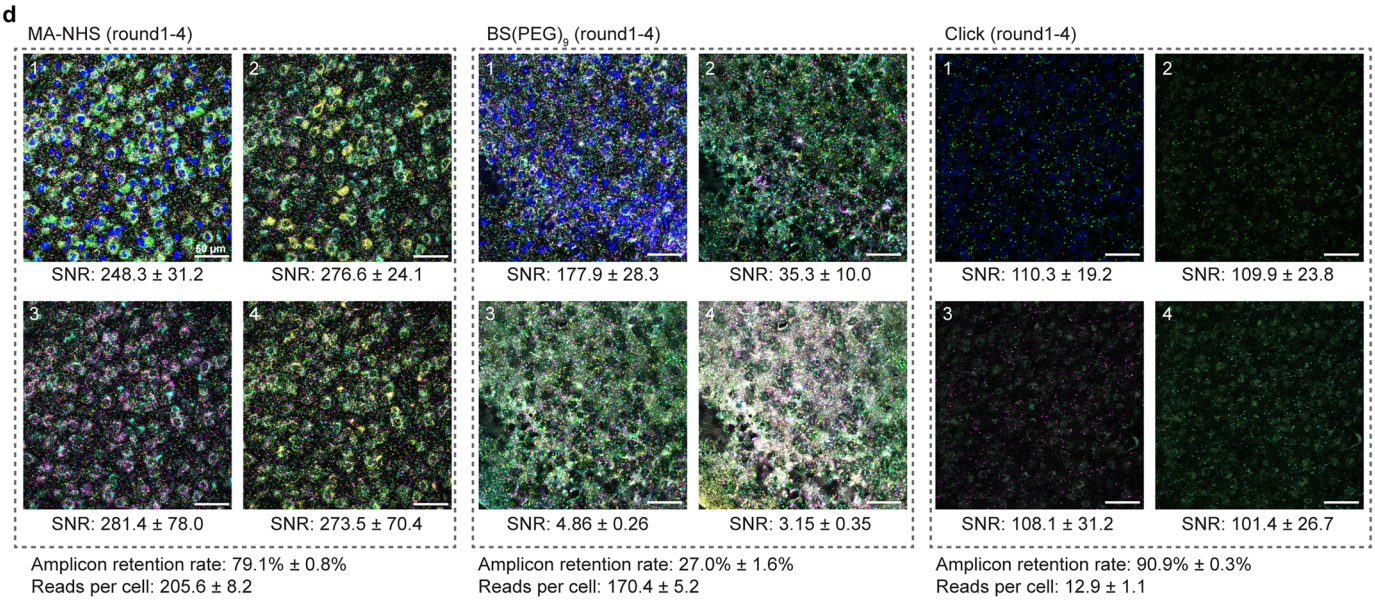

Extended Data Fig. 2 | Optimization of re-embedding strategy. a, Mechanism of cDNA crosslinking using hydrogel re-embedding. Amine-modified nucleotides were incorporated into the rolling-circle amplification reaction. MA-NHS enables rapid conjugation to nucleophilic groups on the amplicons via its NHS ester under mild conditions. These functionalized methacrylamide moieties are then integrated into the hydrogel, effectively immobilizing the cDNA amplicons. **b**, Mechanism of cDNA crosslinking using BSPEG. Amine-modified nucleotides were incorporated into the rolling-circle amplification reaction followed by BSPEG crosslinking, where the NHS esters of BSPEG react with the amino groups on the amplicons. **c**, Mechanism of cDNA crosslinking using Click chemistry. Azide and alkyne groups were incorporated during the RCA process, followed by the addition of copper to catalyze the azide-alkyne cycloaddition, forming a stable triazole ring as a crosslinking method. **d**, Representative fluorescent imaging demonstrating sequencing signal-to-noise ratio using different cDNA crosslinking strategies. BSPEG and Click chemistry crosslinking result in higher background noise compared to hydrogel re-embedding after several rounds of sequencing. Additionally, the incorporation of azide and alkyne moieties during RCA significantly reduced amplification efficiency, leading to fewer amplicons. SNR is defined as the ratio of signal intensity to background intensity. $n = 4$ biological replicates per condition. Data presented as mean ± standard deviation.

https://doi.org/10.1038/s41592-025-02867-0

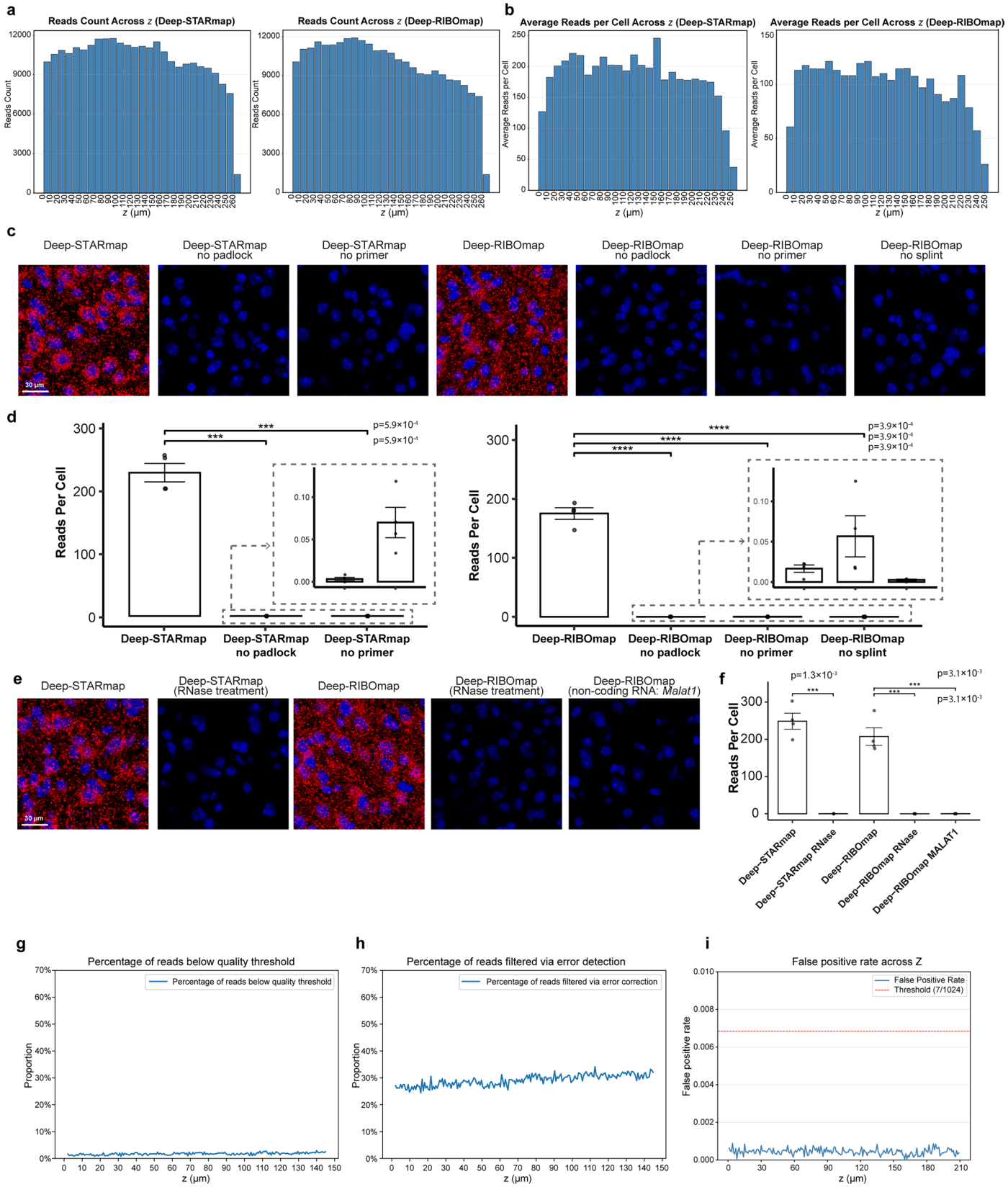

Extended Data Fig. 3 | See next page for caption.

https://doi.org/10.1038/s41592-025-02867-0

Extended Data Fig. 3 | Detection specificity, depth-dependent transcript quantification, and sequencing quality assessment in Deep-STARmap and Deep-RIBOmap. a, Total read counts for 4 cell-type markers (Supplementary Table 1) as a function of tissue depth in 260-µm-thick mouse brain slices processed with Deep-STARmap (left) and Deep-RIBOmap (right). Read counts remain stable within the first 200 µm but progressively decline beyond this depth, dropping below ~75% of the initial counts at 250 µm. **b**, Average reads per cell for the same 4 cell-type markers as a function of tissue depth in Deep-STARmap (left) and Deep-RIBOmap (right). **c**, Representative fluorescent images showing DNA amplicons from 4 cell-type markers (Supplementary Table 1) (red) and nuclei (DAPI, blue) in Deep-STARmap and Deep-RIBOmap under different control conditions. Scale bar: 30 µm. **d**, Quantification of reads per cell for each condition, demonstrating significantly reduced signal in the absence of required probe components. Inset panels show zoomed-in views of low-signal conditions. Statistical analysis was performed using a two-sided t-test, with ***P < 0.001 and ****P < 0.0001. Data are presented as mean ± standard deviation from $n = 4$ technical replicates per condition. **e**, Representative fluorescence images of RNA amplicons (red) and nuclei (DAPI, blue) under various control conditions using four neuron markers (Supplementary Table 1). **f**, Quantification of reads per cell across all conditions. Bars represent mean ± s.d.; n = 4 technical replicates per condition. ***P < 0.001, two-sided t-test. Scale bar, 30 µm. **g**, Proportion of reads filtered due to low-quality scores across *z*-depth. **h**, Proportion of reads filtered out due to sequencing errors (not CXXXXXC) across *z*-depth. **i**, False positive rate estimation using 7 unused barcodes. The detected false positive rate (blue line) remains significantly below the theoretical threshold (red dashed line) across Z-depth.

https://doi.org/10.1038/s41592-025-02867-0

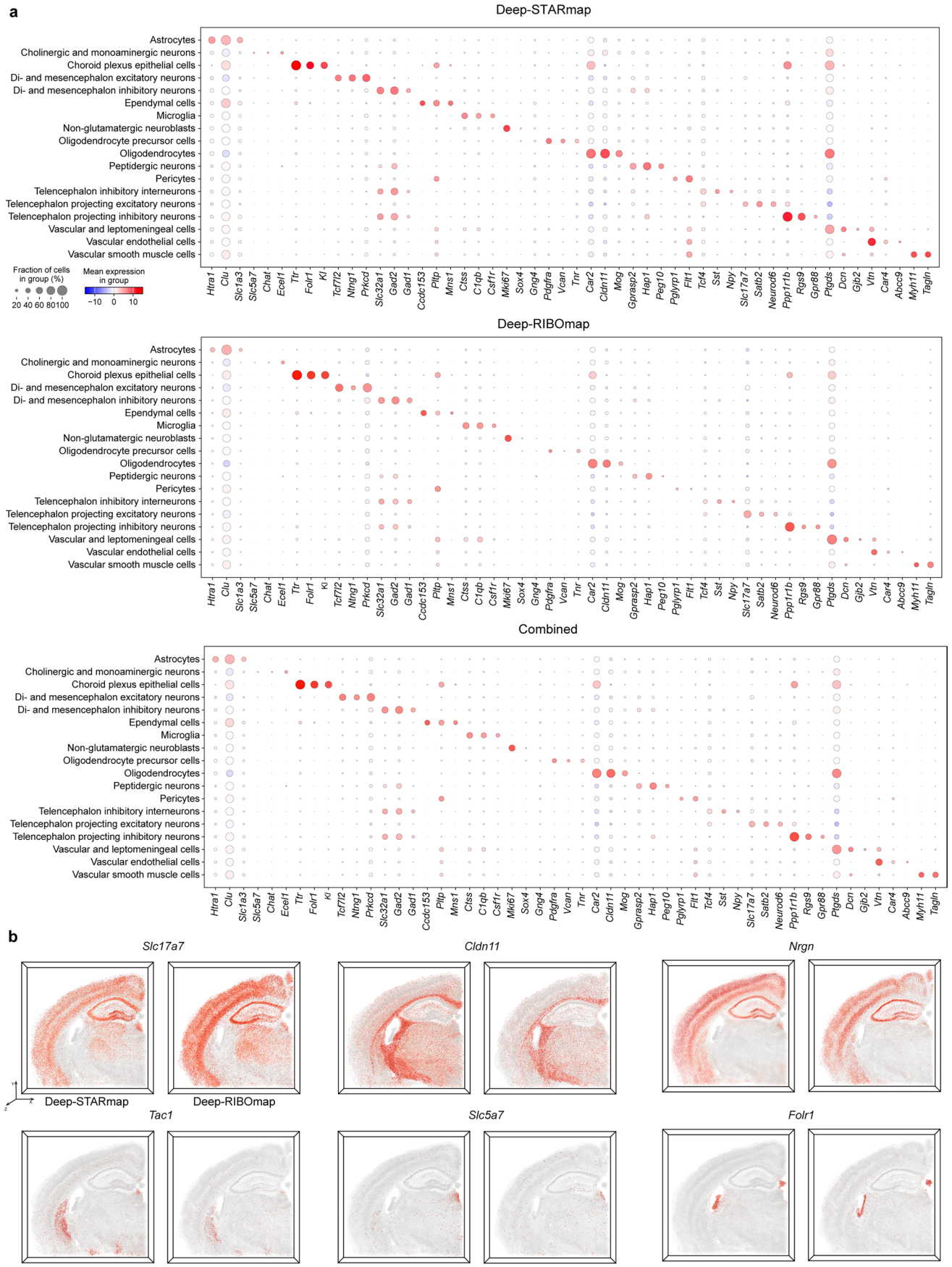

Extended Data Fig. 4 | Single-cell spatial transcriptomic and translatomic profiling of 1,017 genes in the mouse brain. a, Dot plot illustrating the expression levels of representative markers across various major cell types. The color scale represents the $\log_2$ fold change in gene expression compared to the mean gene expression values across all cells. The dot size indicates the percentage of cells expressing the genes within each major cell type. **b**, Deep-STARmap (left) and Deep-RIBOmap (right) images of example cell marker genes and neurotransmitter genes. xyz size: 4.5 mm, 4.5 mm, 150 µm.

https://doi.org/10.1038/s41592-025-02867-0

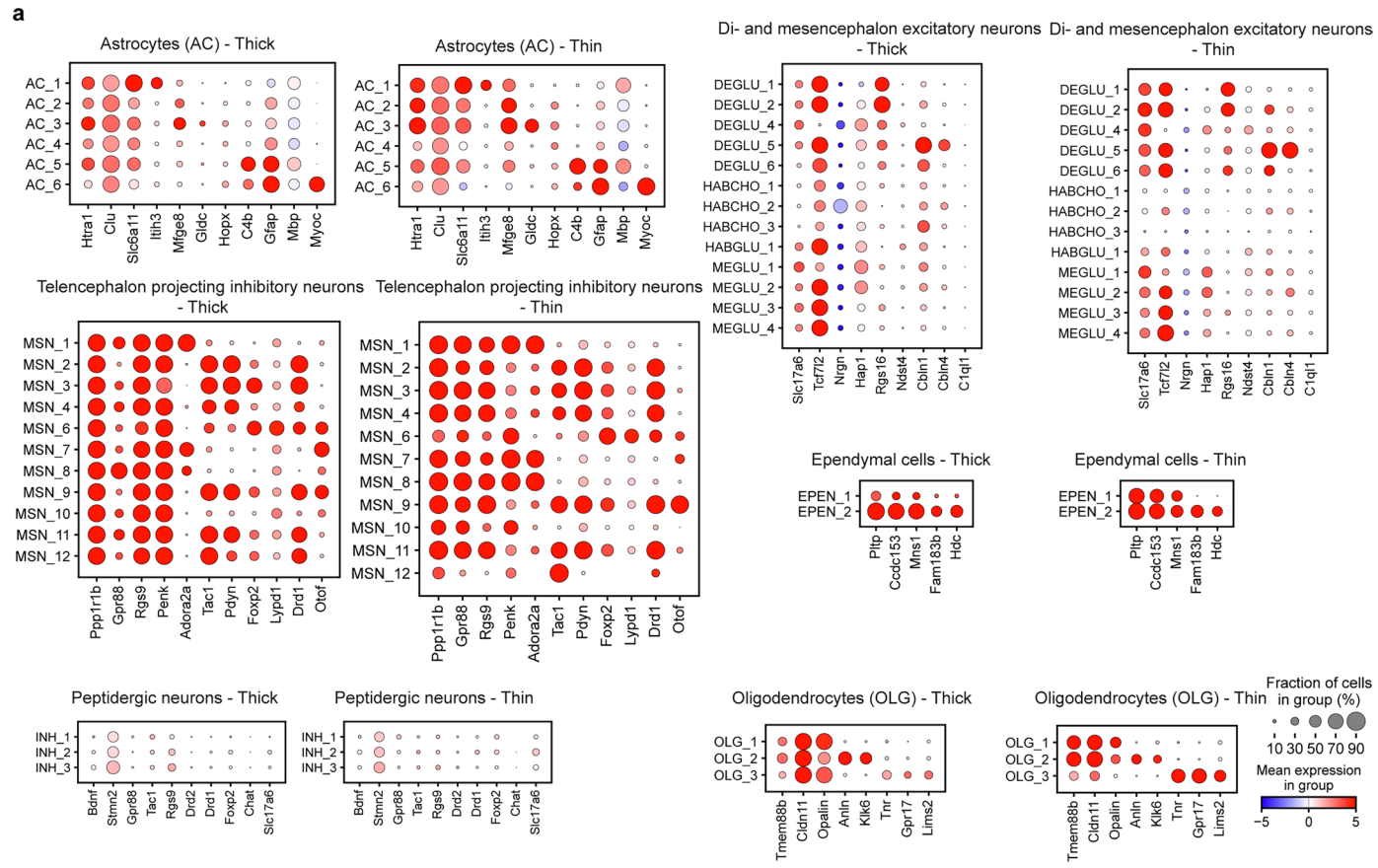

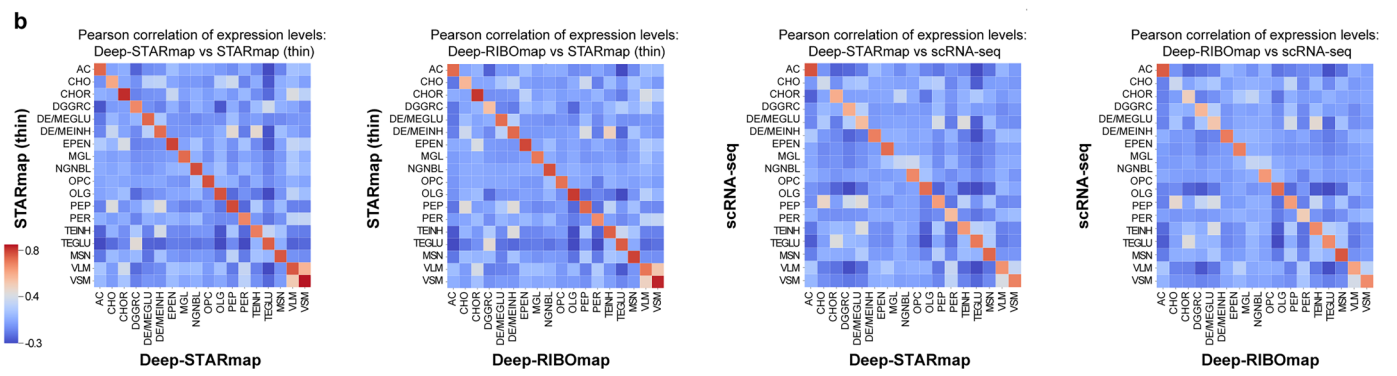

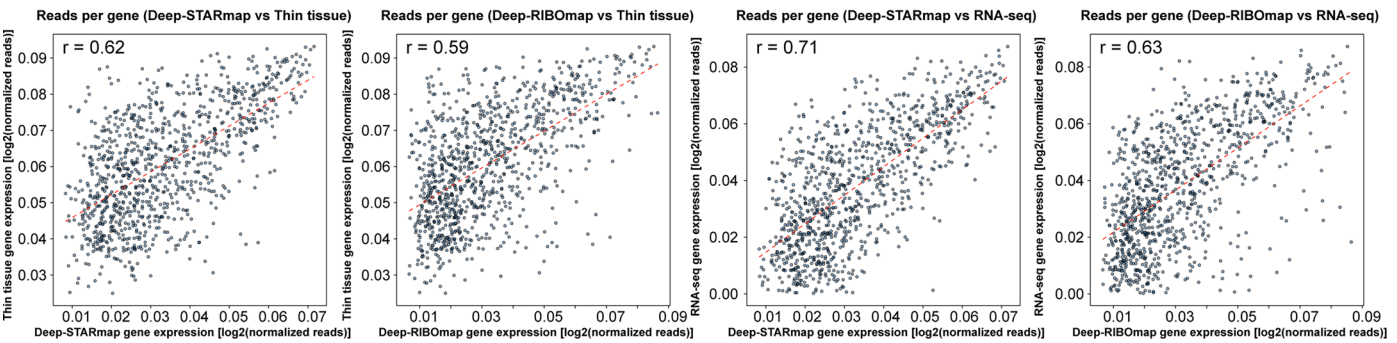

Extended Data Fig. 5 | See next page for caption.

https://doi.org/10.1038/s41592-025-02867-0

Extended Data Fig. 5 | Marker gene expression and cross-modal correlation analysis. a, Dot plot showing marker gene expression across astrocytes (AC), oligodendrocytes (OLG), di- and mesencephalon excitatory neurons (DEGLU, HABCHO, HABGLU, MEGLU), peptidergic neurons (INH), telencephalon projecting inhibitory neurons (MSN), and ependymal cells (EPEN) in thick and thin sections. The color scale represents the $\log_2$ fold change in gene expression compared to the mean gene expression values across all cells. The dot size indicates the percentage of cells expressing the genes within each major cell type. **b**. Pearson correlation heatmaps comparing gene expression profiles across modalities. Left two panels: correlation between Deep-STARmap or Deep-RIBOmap and thin-section STARmap. Right two panels: correlation between Deep-STARmap or Deep-RIBOmap and reference scRNA-seq profiles. Each matrix shows cell-type-level average gene expression correlation. **c**. Scatter plots comparing average gene expression levels between spatial methods and bulk RNA-seq from mouse cortex. Left two panels: correlation of gene expression between Deep-STARmap or Deep-RIBOmap and thin tissue STARmap. Right two panels: correlation with bulk RNA-seq. Each dot represents one gene. Gene expression values are $\log_2$-transformed and normalized. Pearson correlation coefficients (r) are reported in each plot; red dashed lines indicate the identity line.

https://doi.org/10.1038/s41592-025-02867-0

Extended Data Fig. 6 | Spatial organization of fine-grained neuronal, oligodendrocyte, and astrocyte clusters in thick and thin tissue sections. **a**, Spatial distribution of TEGLU (Telencephalon projecting excitatory neurons), OLG (oligodendrocyte), AC (astrocyte), DEGLU (Di- and mesencephalon excitatory neurons), and INH (Di- and mesencephalon inhibitory neurons) subtypes in coronal mouse brain sections, shown for both thick and thin tissue preparations.

https://doi.org/10.1038/s41592-025-02867-0

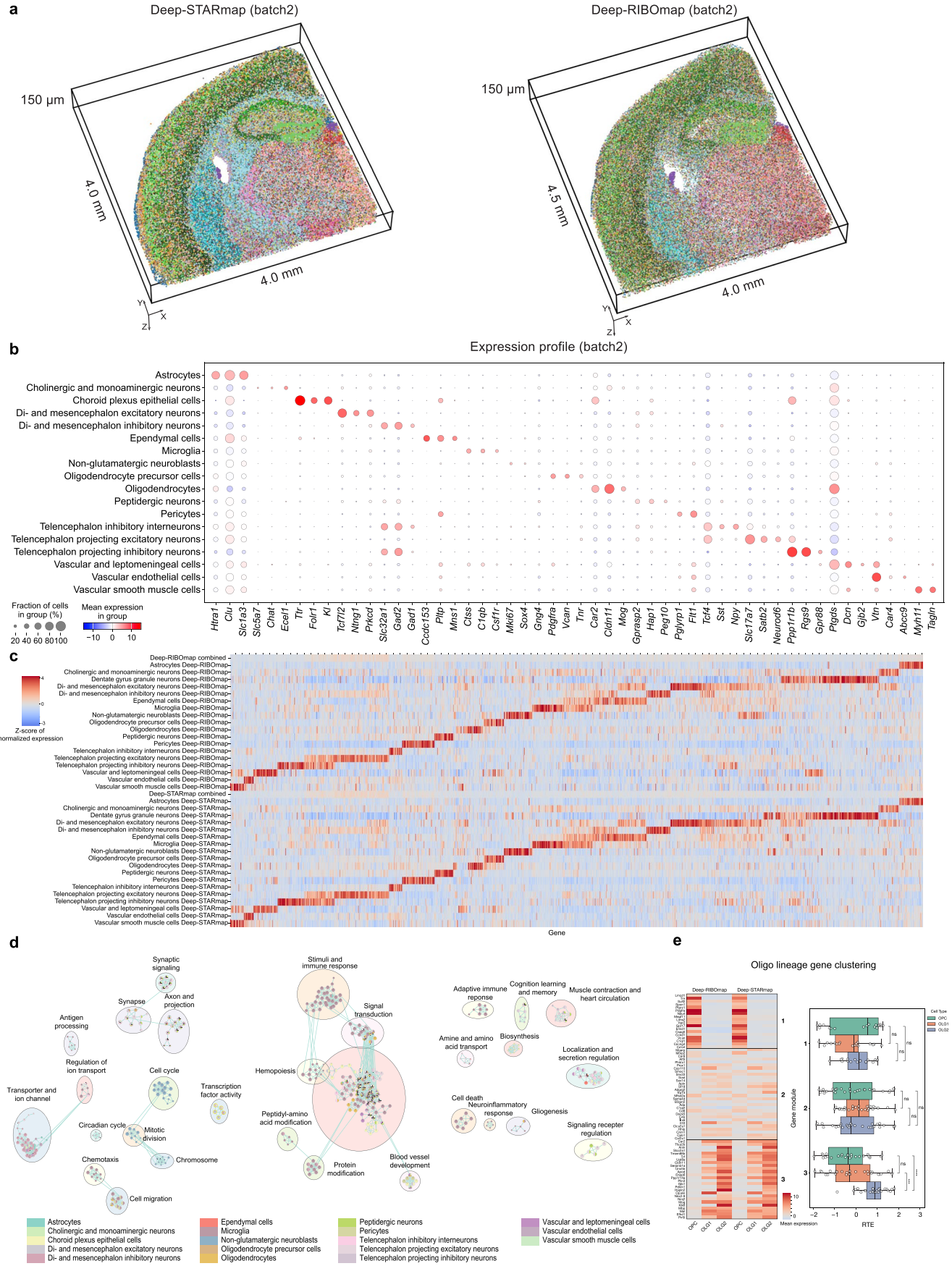

Extended Data Fig. 7 | See next page for caption.

https://doi.org/10.1038/s41592-025-02867-0

Extended Data Fig. 7 | Reproducibility of Deep-STARmap and Deep-RIBOmap, spatial translatome-transcriptome comparison. a, 3D molecular cell-type maps of two independent biological replicates for Deep-STARmap (left) and Deep-RIBOmap (right) in 150-µm-thick coronal mouse brain sections. Each dot represents an individual cell, colored by its assigned cell type. **b**, Dot plot visualization of gene expression profiles across major cell types in batch 2. The color scale represents the $\log_2$ fold change in gene expression compared to the mean gene expression values across all cells. The dot size indicates the percentage of cells expressing the genes within each major cell type. **c**, Heat map showing the gene clustering using the RIBOmap and STARmap results by cell type (Z-score expression). **d**, Visualization of enriched GO terms within each gene module, categorized and color-coded by module. In the enrichment map, nodes represent enriched GO terms, with the size of each node reflecting the number of genes associated with that term. Edges between nodes indicate shared genes among the GO terms. **e**, Heat map displaying gene clustering based on Deep-STARmap and Deep-RIBOmap results across the three oligodendrocyte lineage cell types (left). The right panel shows the relative translational efficiency (RTE) of these genes within each oligodendrocyte lineage cell type (Z-score expression). Statistical significance was assessed using pairwise Mann-Whitney U tests with Benjamini-Hochberg FDR correction. Sample sizes: gene module 1 ($n = 18$), Gene module 2 ($n = 30$), Gene module 3 ($n = 26$).

https://doi.org/10.1038/s41592-025-02867-0

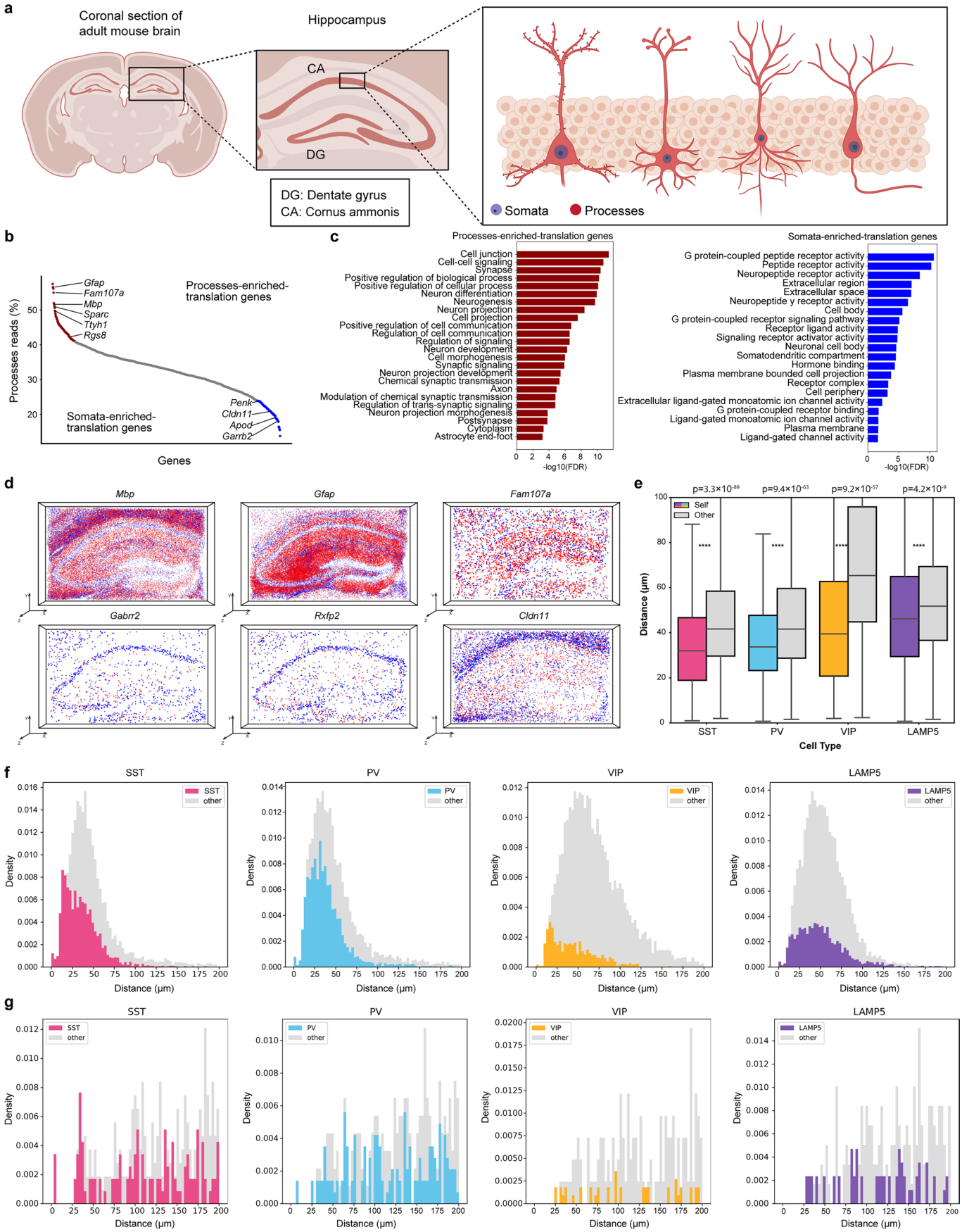

Extended Data Fig. 8 | See next page for caption.

https://doi.org/10.1038/s41592-025-02867-0

Extended Data Fig. 8 | Localized translation in the somata and processes of neuronal and glial cells in the mouse brain. a, Schematic illustration of a hippocampal slice highlighting the somata and processes of hippocampal neurons. **b**, Processes read percentages of individual translating genes with genes rank-ordered based on their process reads percentage. **c**, Significantly enriched GO terms for processes-enriched and somata-enriched translating genes. **d**, Spatial translation map of representative genes with enriched translation in processes (top) and somata (bottom) within the hippocampus, depicting somata reads in blue and process reads in red. **e**, **f**, Nearest-neighbor distance distributions from SST, PV, VIP, and LAMP5 neurons to cells of the same subtype ('to self') and to other inhibitory subtypes ('to other') in a single Deep-STARmap sample (SST: n = 3,027; PV: n = 3,280; LAMP5: n = 1,985; VIP: n = 1,073). Center line, median; box bounds, interquartile range (IQR: 25th to 75th percentile); whiskers, 1.5×IQR; outliers excluded. Two-sided independent *t*-test, ****P < 0.0001. **g**, Nearest-neighbor distance distributions in 15-μm thin sections subsampled from the same 3D Deep-STARmap volume. Binwidth = 3 μm. The y-axis shows probability density, where the area under the entire histogram equals 1.

https://doi.org/10.1038/s41592-025-02867-0

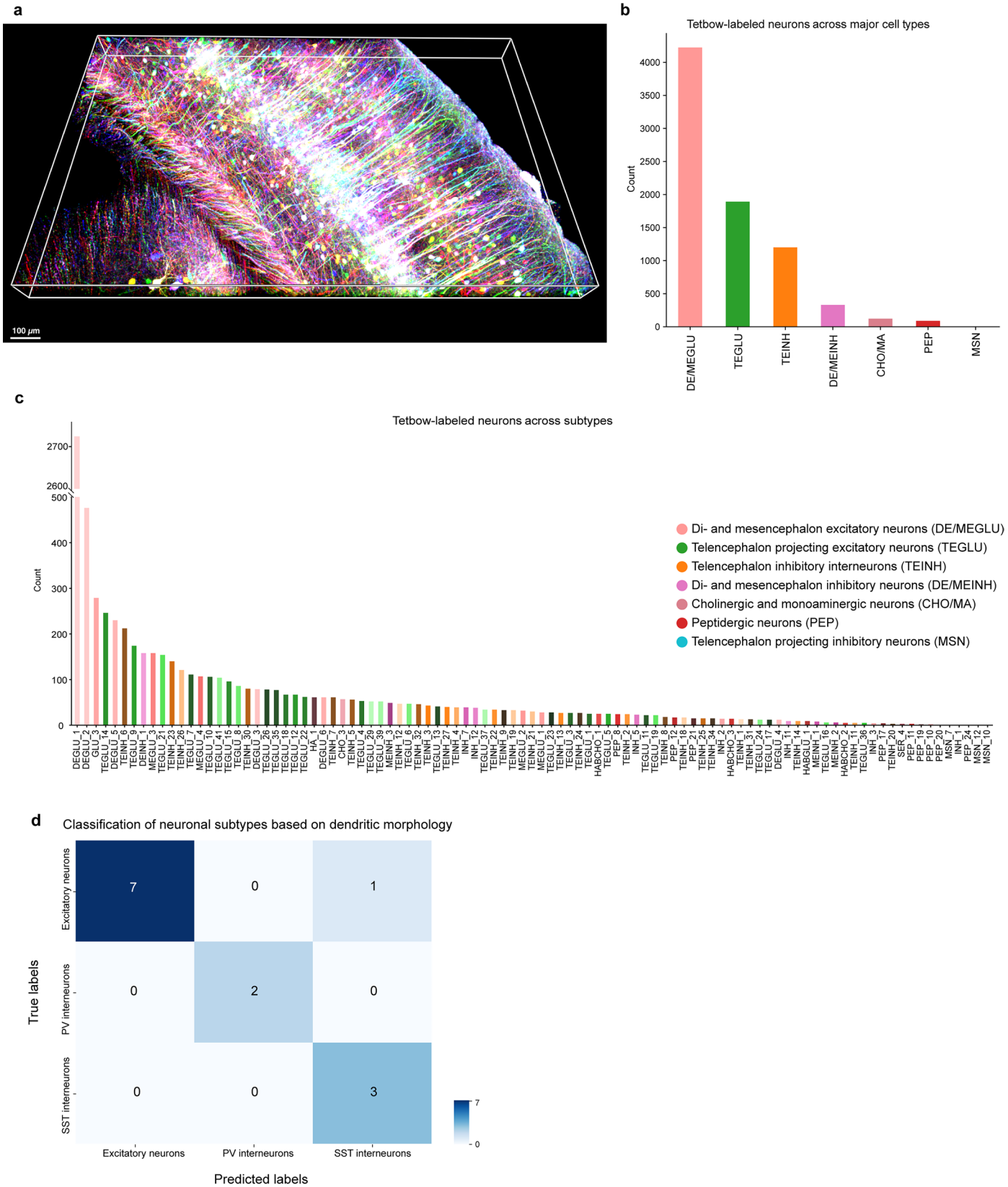

Extended Data Fig. 9 | Quantification of Tebow-labeled neurons. a, Another zoom-in view of volume rendering of mouse cortical pyramidal neurons labeled with Tetbow. **b**, **c**, Cell count quantification of Tebow-labeled neurons across major cell types (b) and subtypes (c). **d**, Confusion matrix showing the performance of a classifier trained on morphological features of reconstructed neurons. The classifier distinguishes excitatory neurons, Pv interneurons, and Sst interneurons with high accuracy. The y-axis represents true neuronal subtypes, and the x-axis indicates predicted labels. Values in each cell correspond to the raw number of neurons assigned to each category.

https://doi.org/10.1038/s41592-025-02867-0

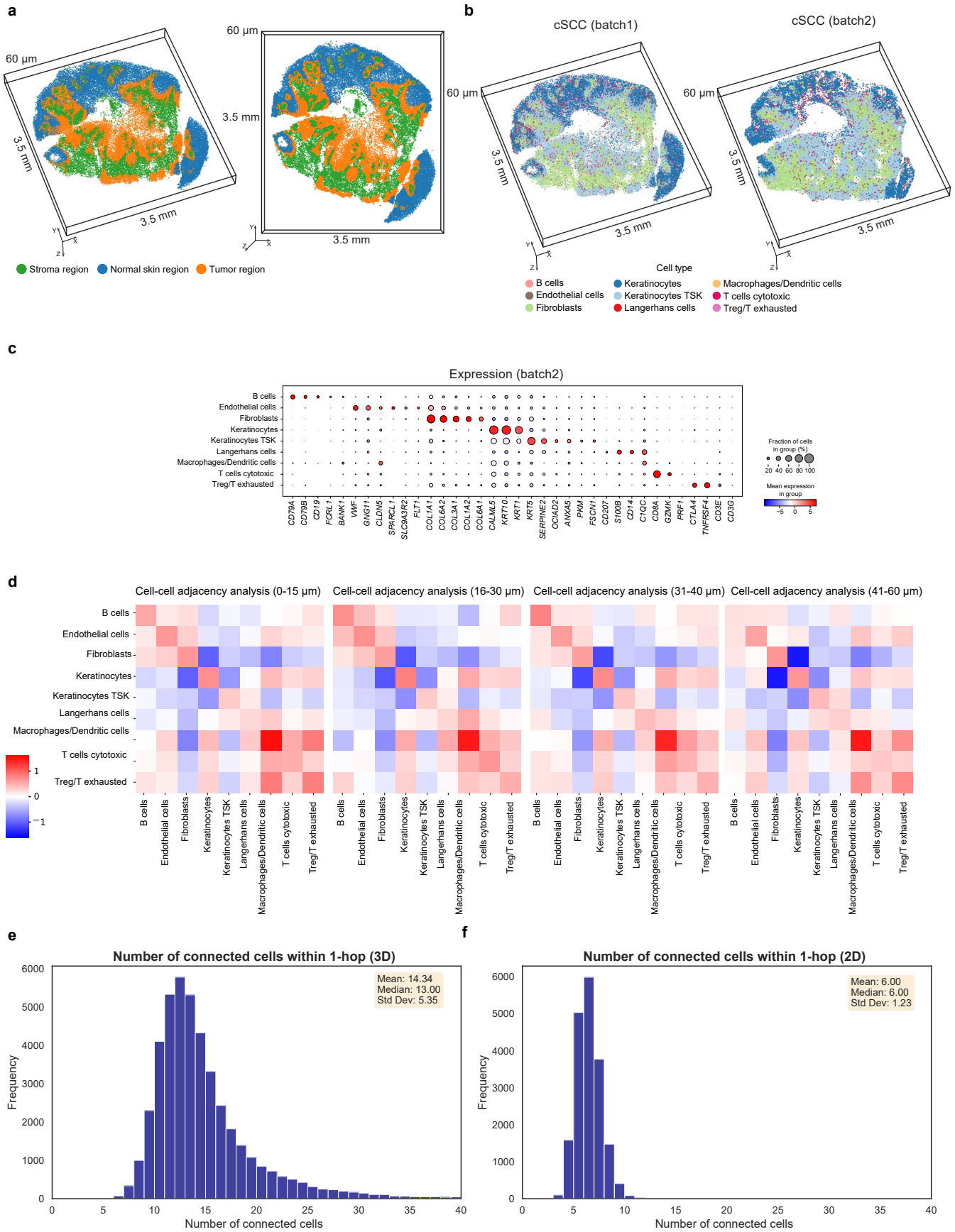

Extended Data Fig. 10 | See next page for caption.

https://doi.org/10.1038/s41592-025-02867-0

Extended Data Fig. 10 | 3D spatial mapping of molecular regions, cell types, gene expression, and cell–cell adjacency analysis in cSCC. a, Molecular tissue region maps visualized in 3D. Each dot represents a cell. Three molecular regions can be identified: tumor, fibroblast-rich stroma, and normal skin. These regions were identified by analyzing low-frequency, large-scale patterns within the spatial neighbors graph. **b**, 3D spatial distribution of cell types in two independent cSCC tumor sections from the same patient, mapped using Deep-STARmap. **c**, Gene expression profiles of marker genes across major cell types in the replicate. The color scale represents the $\log_2$ fold change in gene expression compared to the mean gene expression values across all cells. The dot size indicates the percentage of cells expressing the genes within each major cell type. **d**, 2D cell–cell adjacency quantified in 4 different 15 µm subslices by log enrichment, calculated as the logarithm of the ratio of observed adjacency frequency to the mean adjacency frequency from 1,000 permutations. The 2D analysis is performed by projecting 15 µm (~1 cell layer) slices along the *z*-axis, taken within the same 3D volume as shown in Fig. 4. **e**, **f**, The 3D analysis detects stronger patterns of cell–cell adjacencies because the number of connected cells (edges of a given cell in the mesh graph via Delaunay triangulation) is greater than in 2D. The 2D nearest-neighbor distances cannot accurately represent the 3D cellular environment.

nature portfolio

Corresponding author(s): Xiao Wang

Last updated by author(s): Jul 1, 2025

Reporting Summary

Nature Portfolio wishes to improve the reproducibility of the work that we publish. This form provides structure for consistency and transparency in reporting. For further information on Nature Portfolio policies, see our Editorial Policies and the Editorial Policy Checklist.

Statistics

For all statistical analyses, confirm that the following items are present in the figure legend, table legend, main text, or Methods section.

n/a	Confirmed
☐	☒ The exact sample size (*n*) for each experimental group/condition, given as a discrete number and unit of measurement
☐	☒ A statement on whether measurements were taken from distinct samples or whether the same sample was measured repeatedly
☐	☒ The statistical test(s) used AND whether they are one- or two-sided *Only common tests should be described solely by name; describe more complex techniques in the Methods section.*
☒	☐ A description of all covariates tested
☐	☒ A description of any assumptions or corrections, such as tests of normality and adjustment for multiple comparisons
☐	☒ A full description of the statistical parameters including central tendency (e.g. means) or other basic estimates (e.g. regression coefficient) AND variation (e.g. standard deviation) or associated estimates of uncertainty (e.g. confidence intervals)
☒	☐ For null hypothesis testing, the test statistic (e.g. *F*, *t*, *r*) with confidence intervals, effect sizes, degrees of freedom and *P* value noted *Give P values as exact values whenever suitable.*
☒	☐ For Bayesian analysis, information on the choice of priors and Markov chain Monte Carlo settings
☒	☐ For hierarchical and complex designs, identification of the appropriate level for tests and full reporting of outcomes
☒	☐ Estimates of effect sizes (e.g. Cohen's *d*, Pearson's *r*), indicating how they were calculated

Our web collection on statistics for biologists contains articles on many of the points above.

Software and code

Policy information about availability of computer code

Data collection	Leica LAS-X microscope imaging software was used during data acquisition. Huygens 23.4.0 was used for image deconvolution.
Data analysis	Deep-STARmap and Deep-RIBOmap are implemented based on MATLAB v.R2023b, Python v.3.8 and R v.4.2.1. The data processing tool has been deposited to Zenodo.

For manuscripts utilizing custom algorithms or software that are central to the research but not yet described in published literature, software must be made available to editors and reviewers. We strongly encourage code deposition in a community repository (e.g. GitHub). See the Nature Portfolio guidelines for submitting code & software for further information.

Data

Policy information about availability of data

All manuscripts must include a data availability statement. This statement should provide the following information, where applicable:

- Accession codes, unique identifiers, or web links for publicly available datasets
- A description of any restrictions on data availability
- For clinical datasets or third party data, please ensure that the statement adheres to our policy

The TEMPOmap sequencing data are available on the Single Cell Portal (https://singlecell.broadinstitute.org/single_cell/study/SCP1792) and can be accessed with the following credential (for reviewers only, Accession: SCP1792, URL: https://singlecell.broadinstitute.org/single_cell/reviewer_access/3d65b9ff-3cae-4d12-9cde-a586da081c16, PIN: E5CNEQJELB).
TEMPOmap analysis tool will be maintained and updated at https://github.com/wanglab-broad/TEMPOmap.

Field-specific reporting

Please select the one below that is the best fit for your research. If you are not sure, read the appropriate sections before making your selection.

☒ Life sciences ☐ Behavioural & social sciences ☐ Ecological, evolutionary & environmental sciences

For a reference copy of the document with all sections, see nature.com/documents/nr-reporting-summary-flat.pdf

Life sciences study design

All studies must disclose on these points even when the disclosure is negative.

Sample size	Experiments were applied on 41,4175 cells in total.
Data exclusions	See Methods section: Data processing for Deep-STARmap and Deep-RIBOmap
Replication	Major findings in Deep-STARmap and Deep-RIBOmap dataset were drawn from one biological replicate.
Randomization	N/A.
Blinding	N/A.

Reporting for specific materials, systems and methods

We require information from authors about some types of materials, experimental systems and methods used in many studies. Here, indicate whether each material, system or method listed is relevant to your study. If you are not sure if a list item applies to your research, read the appropriate section before selecting a response.

Materials & experimental systems

n/a	Involved in the study
☒	☐ Antibodies
☐	☒ Eukaryotic cell lines
☒	☐ Palaeontology and archaeology
☐	☒ Animals and other organisms
☐	☒ Human research participants
☒	☐ Clinical data
☒	☐ Dual use research of concern

Methods

n/a	Involved in the study
☒	☐ ChIP-seq
☒	☐ Flow cytometry
☒	☐ MRI-based neuroimaging

Eukaryotic cell lines

Policy information about cell lines

Cell line source(s)	Human HeLa cell line used in this study was purchased from ATCC (CCL-2, lot 70016358).
Authentication	The cell line has been authenticated by the STR method.
Mycoplasma contamination	The cell lines were confirmed as mycoplasma negative by DAPI (4",6-diamidino-2-phenylindole) or Hoechst DNA staining and microscope imaging.
Commonly misidentified lines (See ICLAC register)	None.

Animals and other organisms

Policy information about studies involving animals; ARRIVE guidelines recommended for reporting animal research

Laboratory animals	C57/BL6 female mice aged between 6 to 10 weeks
Wild animals	N/A.
Field-collected samples	N/A.
Ethics oversight	Institutional Animal Care and Use Committee (IACUC) of the Broad Institute of MIT and Harvard, under animal protocol #0255-08-19

Note that full information on the approval of the study protocol must also be provided in the manuscript.

Human research participants

Policy information about studies involving human research participants

Population characteristics	Discarded human squamous cell carcinoma tissue from patient Mohs micrographic surgeries were obtained from Massachusetts General Hospital. All human skin cancer samples were fully deidentified prior to use, with the removal of patient identifiers and demographic data to protect subject confidentiality in accordance with institutional guidelines.
Recruitment	Consent for use of discarded tissue was obtained from patients receiving Mohs micrographic surgery treatment for skin cancer. Participation had no impact on treatment.
Ethics oversight	Massachusetts General Hospital IRB (protocol 2013P000093)

Note that full information on the approval of the study protocol must also be provided in the manuscript.